drones

MDPI

Article

Robust Attitude Control of Fixed-Wing UAVs Under Near-Envelope Conditions Using a Hierarchical Adaptive NSGA-II

Wanli Chen [1,2], Shijun Guo [2,3], Xinyu Li [2,3], Song Wang [1,*], Zhiqiang Wan [1], Xishuo Jia [1] and Zhuoer Yao [4]

[1] School of Aeronautic Science and Engineering, Beihang University, Beijing 100191, China; chenwanli@buaa.edu.cn (W.C.); wzq@buaa.edu.cn (Z.W.); jiaxs1013@buaa.edu.cn (X.J.)
[2] Institute of Engineering Thermophysics, Chinese Academy of Sciences, Beijing 100190, China; guoshijun@iet.cn (S.G.); lixinyu@iet.cn (X.L.)
[3] School of Space Exploration, University of Chinese Academy of Sciences, Beijing 100049, China
[4] Hangzhou International Innovation Institute, Beihang University, Hangzhou 311115, China; yzebuaa@buaa.edu.cn
* Correspondence: wangsongking@buaa.edu.cn

Highlights

What are the main findings?

- To address the multi-objective controller-parameter optimization challenge faced by fixed-wing UAVs under near-envelope conditions, this study proposes a two-stage architecture combining hierarchical single-objective pre-optimization and multi-objective coordinated optimization, which accounts for the main reduction in comprehensive fitness relative to standard NSGA-II (approximately 4.41%).
- A threefold adaptive mechanism covering parameter ranges, crossover and mutation probabilities, and objective weights is integrated into the optimization framework, mainly lowering the post-convergence coefficient of variation from 0.0020 to 0.0006 and providing a further 0.083% reduction in final fitness relative to hierarchical pre-optimization alone.

What are the implications of the main findings?

- This work provides an engineering-feasible offline parameter-optimization approach for nonlinear control of fixed-wing UAVs under the tested near-envelope conditions without changing the existing controller architecture.
- The optimized LADRC remains stable within the tested aerodynamic parameter perturbation ranges and maintains attitude-tracking performance. Flight-test results support implementation on the tested platform.

Abstract

To address the strong aerodynamic coupling and insufficient control robustness of fixed-wing unmanned aerial vehicles (UAVs) under near-envelope conditions, this study focuses on three-axis attitude stabilization and develops a two-level control architecture consisting of an attitude/load-factor stability-augmentation loop and an angular-rate stability-augmentation loop. The outer loop adopts an attitude-angle dynamic-inversion and load-factor correction structure, whereas the inner loop employs linear active disturbance rejection control (LADRC). An improved non-dominated sorting genetic algorithm II (NSGA-II) integrating hierarchical pre-optimization and a threefold adaptive mechanism is proposed for multi-objective controller-parameter tuning. Hierarchical

Academic Editor: Yajie Ma

Received: 17 May 2026
Revised: 7 July 2026
Accepted: 10 July 2026
Published: 13 July 2026

single-objective pre-optimization is followed by multi-objective coordinated optimization to reduce premature convergence in high-dimensional parameter optimization. A threefold adaptive mechanism comprising parameter-range adaptation, crossover and mutation probability adaptation, and objective-weight adaptation balances global exploration and local convergence. Nonlinear simulations and field tests show that hierarchical pre-optimization accounts for the main fitness reduction relative to standard NSGA-II (approximately 4.41%), whereas the adaptive mechanism lowers the post-convergence coefficient of variation from 0.0020 to 0.0006 and adds a 0.083% reduction beyond hierarchical pre-optimization alone. Under combined multi-source perturbations in aerodynamic, inertial, and actuator parameters, the optimized three-channel closed-loop controller remains stable within the tested ranges and maintains attitude-tracking performance. This study supports offline tuning under the tested near-envelope conditions.

Keywords: complex boundary conditions; linear active disturbance rejection control (LADRC); multi-objective genetic algorithm; hierarchical pre-optimization; adaptive optimization; attitude control

1. Introduction

As fixed-wing unmanned aerial vehicles (UAVs) are increasingly used in civilian applications such as surveying and mapping, logistics, and emergency rescue in harsh environments including mountainous valleys and offshore meteorological observation areas, they may encounter strong convection and severe wind-shear gusts that force operation near the flight-envelope boundary. Under these conditions, strong lateral–longitudinal aerodynamic cross-coupling and nonlinear aerodynamic damping degradation may cause nonlinear instability and insufficient control margins. Ensuring flight safety in complex environments therefore requires control schemes with strong disturbance-rejection capability.

Compared with conventional proportional–integral–derivative (PID) controllers, linear active disturbance rejection control (LADRC) offers advantages in handling nonlinear dynamics and aerodynamic perturbations through real-time lumped-disturbance compensation by a linear extended state observer (LESO). For aerodynamic parameter perturbations caused by complex airflow disturbances, LADRC can achieve stable wide-envelope control through dynamic compensation [0]. Its modular structure and disturbance-compensation mechanism are inherently well suited to this application, while the tracking differentiator (TD) can generate a smooth transition process for attitude commands and reduce step-induced transients [2,3]. However, large aerodynamic parameter perturbations and strong multichannel coupling make it difficult for manually tuned parameters to maintain stable control throughout the flight envelope, motivating the use of optimization algorithms for global parameter tuning [4,5]. Population-based optimization algorithms offer multi-objective global-search capability without requiring changes to the original controller architecture and have been widely used for control-parameter optimization [6,7]. Given the multiple constraints of UAV attitude control, the non-dominated sorting genetic algorithm II (NSGA-II), with fast non-dominated sorting and elitist preservation, is well suited to multi-objective optimization and has been widely applied [8,9]. However, standard NSGA-II may exhibit premature convergence, relatively slow convergence, and reduced ability to select high-quality individuals when optimizing high-dimensional flight-control parameters.

https://doi.org/10.3390/drones10070532

To address these limitations, researchers have proposed improvements from several perspectives. Multi-population partitioning and enhanced crossover mechanisms are commonly used to increase the diversity of the non-dominated solution set and mitigate premature convergence [10–12]. Adaptive evolutionary operators and hybrid local optimization have also been investigated to improve convergence while retaining elite solutions [13–16]. To address selection degradation in high-dimensional objective spaces, algorithms such as NSGA-III introduce reference points or objective importance vectors [17–19]. Although these methods improve general-purpose optimization, limitations remain in flight-control parameter optimization. First, population initialization does not fully incorporate the aircraft's aerodynamically feasible region, producing many individuals with limited engineering relevance. Second, adaptive adjustment does not cover all adaptation dimensions, making global exploration and local convergence difficult to balance. Third, coordinated optimization of objective weights and control performance remains insufficient for near-envelope scenarios with multiple constraints and strong disturbances.

In aircraft attitude-control optimization, pigeon-inspired optimization (PIO), particle swarm optimization (PSO), and genetic algorithms have been applied to robust UAV parameter tuning and multimodal control-architecture optimization [20–23]. Recent studies have also demonstrated online evolutionary parameter self-tuning during flight [24], while multi-strategy hybrid optimization algorithms have been used to mitigate premature local convergence in high-dimensional nonlinear decoupling problems [25]. However, most studies focus on conventional flight-envelope conditions, and research on multi-objective parameter optimization for UAV attitude controllers under near-envelope conditions in complex meteorological environments remains limited. In particular, tailored algorithms that jointly consider convergence speed, engineering constraints, and multi-objective coordinated optimization are lacking, making it difficult to meet both real-time and stability requirements under boundary conditions.

In summary, this study considers a civilian fixed-wing UAV for complex operational scenarios and focuses on robust three-axis attitude control under near-envelope conditions. A continuous large-bank roll maneuver is selected as the representative verification task. To address aerodynamic damping degradation and strong multichannel coupling, a two-stage improved NSGA-II framework integrating hierarchical single-objective pre-optimization and multi-objective coordinated optimization is developed for parameter tuning of the three-channel LADRC controller. The framework includes a threefold adaptive mechanism comprising controller parameter-range adaptation, crossover and mutation probability adaptation, and objective-weight adaptation. The improved algorithm is evaluated through 30 independent optimization runs, together with field flight tests. The integrated scheme improves attitude-tracking accuracy, dynamic response, and parameter-perturbation rejection in regions with degraded aerodynamic characteristics, providing an engineering reference for the flight-control design of similar fixed-wing UAVs in complex meteorological environments.

2. Nonlinear Flight-Dynamics Modeling of a Fixed-Wing UAV Under Boundary Conditions

To investigate control under strong aerodynamic coupling near the flight-envelope boundary, this section establishes a complete six-degrees-of-freedom nonlinear flight-dynamics model and designs a continuous alternating attitude-recovery maneuver approaching the performance boundary. The model and maneuver provide a high-fidelity simulation benchmark and a near-limit verification scenario for the subsequent three-axis cascaded LADRC design and improved multi-objective optimization.

https://doi.org/10.3390/drones10070532

2.1. Spatial Reference Frames and Transformation Conventions for Large-Attitude Maneuvers

Unlike conventional steady flight, large-attitude maneuvers involve large-angle nonlinear spatial motion. To describe the UAV trajectory, attitude, and force state, the following three reference frames are defined as the basis for calculating the relevant physical quantities:

(1) Earth-fixed frame ($O_g X_g Y_g Z_g$): The north–east–down (NED) coordinate system is adopted and is primarily used to calculate the position and flight-path information of the UAV.

(2) Body-fixed frame ($O_b X_b Y_b Z_b$): The origin is fixed at the center of mass of the UAV. The $O_b X_b$ axis points forward along the nose of the aircraft, and the $O_b Y_b$ axis points toward the right wing. This frame is used to describe the attitude evolution, body-axis angular velocities, and forces acting along the body axes.

(3) Wind frame ($O_w X_w Y_w Z_w$): This frame is established with respect to the free-stream airflow and serves as the aerodynamic reference frame. It is used to describe the motion of the UAV relative to the incoming airflow and to support the calculation of key aerodynamic parameters.

The transformation relationships among the coordinate frames and the definitions of the attitude angles are illustrated in Figure 1.

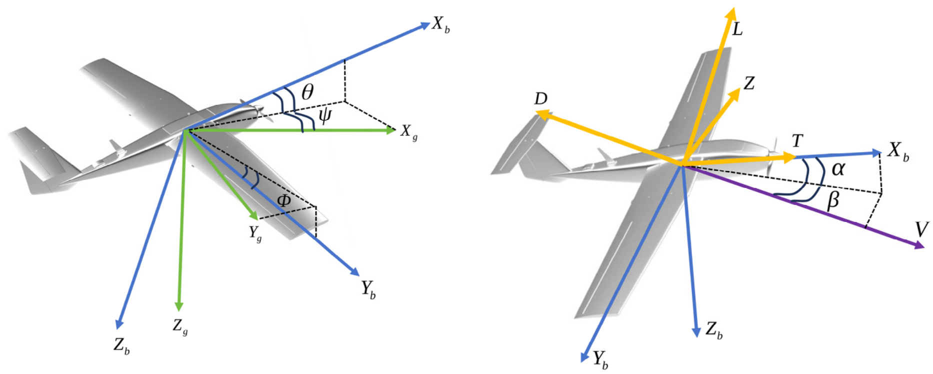

(**a**) (**b**)

Figure 1. Coordinate transformations and attitude-angle definitions for the fixed-wing UAV: (**a**) body-fixed–Earth-fixed transformation; (**b**) wind–body-fixed transformation.

The transformation matrix $T_{\text{gb}}\pi$ from the Earth-fixed frame to the body-fixed frame is given by

$$T_{\text{gb}} = \begin{bmatrix} \cos\theta\cos\psi & \cos\theta\sin\psi & -\sin\theta \\ \sin\theta\sin\Phi\cos\psi - \cos\Phi\sin\psi & \sin\theta\sin\Phi\sin\psi + \cos\Phi\cos\psi & \cos\theta\sin\Phi \\ \sin\theta\cos\Phi\cos\psi + \sin\Phi\sin\psi & \sin\theta\cos\Phi\sin\psi - \sin\Phi\cos\psi & \cos\theta\cos\Phi \end{bmatrix} \tag{1}$$

where Φ, θ, and ψ denote the roll angle, pitch angle, and heading angle (yaw angle), respectively. This matrix directly determines the nonlinear and time-varying characteristics of the projection of the gravitational vector from the Earth-fixed frame onto the body axes.

The transformation matrix T_{wb} from the wind frame to the body-fixed frame is expressed as

$$T_{wb} = \begin{bmatrix} \cos\alpha\cos\beta & -\cos\alpha\sin\beta & -\sin\alpha \\ \sin\beta & \cos\beta & 0 \\ \sin\alpha\cos\beta & -\sin\alpha\sin\beta & \cos\alpha \end{bmatrix}, \tag{2}$$

where α and β denote the angle of attack and sideslip angle, respectively.

Finally, the transformation between the angular velocities in the body-fixed frame and the attitude-angle rates in the Earth-fixed frame is given by

$$\begin{bmatrix} \dot{\Phi} \\ \dot{\theta} \\ \dot{\psi} \end{bmatrix} = \begin{bmatrix} 1 & \sin\Phi\tan\theta & \cos\Phi\tan\theta \\ 0 & \cos\Phi & -\sin\Phi \\ 0 & \sin\Phi/\cos\theta & \cos\Phi/\cos\theta \end{bmatrix} \begin{bmatrix} p \\ q \\ r \end{bmatrix} \tag{3}$$

where p, q, and r denote the roll, pitch, and yaw angular velocities in the body-fixed frame, respectively, while $\dot{\Phi}$, $\dot{\theta}$, and $\dot{\psi}$ denote the corresponding attitude-angle rates. Under large-attitude conditions, the two sets of angular velocities exhibit nonlinear cross-coupling, and conventional decoupled linearized models cannot accurately describe the dynamic evolution of the system.

2.2. Full Nonlinear Flight-Dynamics Modeling Under Near-Flight-Envelope Conditions

Based on the nonlinear coupling characteristics described above and the calculated aerodynamic parameters, the expanded expressions for the aerodynamic forces and moments of the fixed-wing UAV are given by

$$\begin{cases} F_x = \bar{q}S(C_X + C_X^{\delta_e}\delta_e) \\ F_y = \bar{q}S(C_Y + C_Y^{\delta_r}\delta_r) + (\bar{q}/2V)Sb(C_{Yp}p + C_{Yr}r) \\ F_z = \bar{q}S(C_Z + C_Z^{\delta_e}\delta_e) + (\bar{q}/2V)S\bar{c}(C_{Zq}q + C_{Z\dot{\alpha}}\dot{\alpha}) \\ L = \bar{q}Sb(C_l + C_l^{\delta_a}\delta_a) + (\bar{q}/2V)Sb^2(C_{lp}p + C_{lr}r) \\ M = \bar{q}S\bar{c}(C_m + C_m^{\delta_e}\delta_e) + (\bar{q}/2V)S\bar{c}^2(C_{mq}q + C_{m\dot{\alpha}}\dot{\alpha}) \\ N = \bar{q}Sb(C_n + C_n^{\delta_r}\delta_r) + (\bar{q}/2V)Sb^2(C_{np}p + C_{nr}r) \end{cases} \tag{4}$$

where F_x, F_y, and F_z denote the body-axis axial, side, and normal forces, respectively, while L, M, and N denote the roll, pitch, and yaw moments. The quantities $\bar{q}$, V, S, b, and $\bar{c}$ denote the dynamic pressure, airspeed, reference area, reference span, and mean aerodynamic chord, respectively. The variables δ_e, δ_a, and δ_r are the elevator, aileron, and rudder deflections, and $\dot{\alpha}$ is the rate of change in the angle of attack. The coefficients C_X, C_Y, C_Z (force coefficients) and C_l, C_m, C_n (moment coefficients) are the basic dimensionless coefficients of the three body-axis forces and moments, respectively. The superscripts denote control-surface derivatives, whereas the subscripts p, q, r, and $\dot{\alpha}$ denote the corresponding angular-rate and angle-of-attack dynamic derivatives.

Under near-envelope conditions, strong cross-axis coupling and parameter drift make decoupled linear models inadequate for representing the nonlinear aircraft dynamics. Based on the coordinate-transformation matrices, a complete six-degrees-of-freedom nonlinear model comprising 12 first-order state equations arranged in four groups is constructed.

At the spatial kinematics level, the mapping from the body-axis linear velocities to the absolute velocities in the Earth-fixed frame is governed by the instantaneous attitude of the aircraft. The translational kinematic equation is expressed as

$$\left[\dot{x}_g, \dot{y}_g, \dot{z}_g\right] = [u,\ v,\ w]T_{\mathrm{gb}} \tag{5}$$

where $\dot{x}_g$, $\dot{y}_g$, and $\dot{z}_g$ denote the linear-velocity components in the Earth-fixed frame, respectively, and u, v, and w denote the linear-velocity components along the three axes of the body-fixed frame, respectively.

The rotational kinematic equations describe the relationship between the body-axis angular velocities and the spatial evolution of the aircraft attitude. Their complete matrix form has already been given in Equation (3).

At the dynamic level, the translational dynamic equations reveal the nonlinear superposition of aerodynamic forces, thrust, and gravity along the body axes, as well as their coupling with centrifugal inertial forces. According to Newton's second law, the fundamental translational dynamic equations of the UAV in the body-fixed frame can be expressed in the following compact form:

$$\begin{cases} \dot{u} = rv - qw - g\sin\theta + X/m \\ \dot{v} = pw - ru + g\cos\theta\sin\phi + Y/m \\ \dot{w} = qu - pv + g\cos\theta\cos\phi + Z/m \end{cases} \tag{6}$$

where m is the mass of the UAV; g is the gravitational acceleration; $\dot{u}$, $\dot{v}$, and $\dot{w}$ are the linear accelerations along the three body axes; and X, Y, and Z are the resultant forces composed of aerodynamic forces and engine thrust along the three axes of the body-fixed frame, respectively.

To accurately characterize the aerodynamic coupling effects under boundary conditions, the resultant external forces must be explicitly resolved. The gravitational force in the Earth-fixed frame is transformed into the body-fixed frame through the rotation matrix. Meanwhile, the lift L_a, drag D, and side force Y_{aero} in the wind frame are transformed into the body-fixed frame using the rotation matrix T_{wb}. By incorporating the engine thrust T and substituting the resulting forces into Equation (6), the expanded translational dynamics are obtained as:

$$\begin{bmatrix} \dot{u} \\ \dot{v} \\ \dot{w} \end{bmatrix} = \frac{1}{m} \begin{bmatrix} T - D\cos\alpha\cos\beta + L_a\sin\alpha - Y_{\text{aero}}\cos\alpha\sin\beta - mg\sin\theta \\ -D\sin\beta + Y_{\text{aero}}\cos\beta + mg\cos\theta\sin\phi \\ -D\sin\alpha\cos\beta - L_a\cos\alpha - Y_{\text{aero}}\sin\alpha\sin\beta + mg\cos\theta\cos\phi \end{bmatrix} + \begin{bmatrix} vr - wq \\ wp - ur \\ uq - vp \end{bmatrix} \tag{7}$$

Under large angle-of-attack and large sideslip conditions, the aerodynamic forces, thrust, and gravity form nonlinear coupling relationships along the body axes. On the basis of the translational dynamics, the rotational dynamic equations about the center of mass govern the attitude evolution of the UAV. To facilitate the subsequent derivation of the control law, these equations are rearranged into the following standard form containing the inertia-related coefficients:

$$\begin{cases} \dot{p} = (c_1 r + c_2 p)q + c_3 L + c_4 N \\ \dot{q} = c_5 pr - c_6(p^2 - r^2) + c_7 M \\ \dot{r} = (c_8 p - c_2 r)q + c_4 L + c_9 N \end{cases} \tag{8}$$

where $\dot{p}$, $\dot{q}$, and $\dot{r}$ denote the angular accelerations about the three body axes; L, M, and N denote the resultant external roll, pitch, and yaw moments in the body-fixed frame, respectively; and c_1 – c_9 are inertia-related coefficients determined by the moments of inertia I_x, I_y, and I_z about the three body axes and the product of inertia I_{xz}. Their specific definitions are given by: $\Gamma = I_x I_z - I_{xz}^2$, $c_1 = [(I_y - I_z)I_z - I_{xz}^2]/\Gamma$, $c_2 = [(I_x - I_y + I_z)I_{xz}]/\Gamma$, $c_3 = I_z/\Gamma$, $c_4 = I_{xz}/\Gamma$, $c_5 = (I_z - I_x)/I_y$, $c_6 = I_{xz}/I_y$, $c_7 = 1/I_y$, $c_8 = [I_x(I_x - I_y) + I_{xz}^2]/\Gamma$, and $c_9 = I_x/\Gamma$. The product terms in Equation (8) indicate that gyroscopic moments and inertial coupling moments arise across the control channels during high-rate maneuvers.

A conventionally configured fixed-wing UAV is considered in this study. Its principal physical parameters are specified according to the nominal values of an engineering prototype, as listed in Table 1.

Table 1. Basic parameters of the UAV.

Category	Parameter	Value
Mass properties	Takeoff mass	220 kg
	Roll moment of inertia I_x	20 kg·m²
	Pitch moment of inertia I_y	260 kg·m²
	Yaw moment of inertia I_z	252 kg·m²
Flight performance	Cruise speed	100 m/s
	Cruise altitude	4 km
	Maximum speed	150 m/s
	Maximum service ceiling	6 km

An operating condition on the right boundary of the flight envelope was selected for robustness evaluation. A full nonlinear model and high-dimensional aerodynamic matrices were used to represent aerodynamic nonlinearities and lateral–directional coupling in high-precision numerical simulations. The baseline condition was an altitude of 5500 m and an airspeed of 150 m/s, within the high-speed region above 90% of the maximum envelope airspeed shown in Figure 2. The cruise angle of attack was approximately 2–3°, with a 12° stall-angle margin; the maneuver load factor was 3–4 g, and the maximum control-surface deflection was approximately 65% of its physical limit. This near-instability condition approached the performance boundary without reaching the aerodynamic or structural limits.

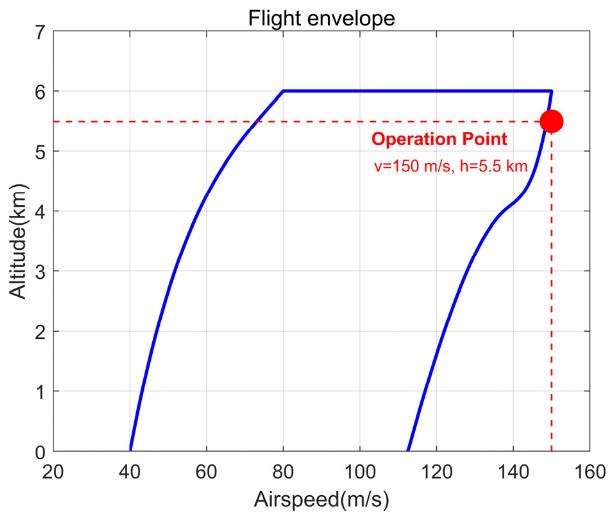

Figure 2. Flight envelope and boundary operating conditions of the UAV.

Near-envelope off-design conditions can cause nonlinear shifts in control effectiveness and stability margins, reducing controller robustness. In the longitudinal channel, near-envelope flow conditions can alter horizontal-tail effectiveness, causing aerodynamic-center shifts and nonlinear changes in pitch damping. Ground effect may also increase horizontal-tail effectiveness and alter the pitch stability margin [26]. Although ground effect is outside the high-altitude, high-speed scope of this study, the general variation in horizontal-tail effectiveness with flight condition provides a theoretical basis for the pitch-channel aerodynamic perturbations. In the lateral–directional channels, large sideslip angles and rudder deflections may induce vertical-tail flow separation, reducing side-force effectiveness and yaw-control margin while increasing nonlinear drag and lateral–directional coupling. The interaction between sideslip and rudder deflection may also cause vertical-tail aerodynamics to depart from linear assumptions [27]. Accordingly, ±80% perturbations and sign reversals were applied to the lateral–directional aerodynamic derivatives in the robustness tests to maintain engineering relevance and physical plausibility.

Increased near-envelope coupling and shifts in control characteristics make it difficult for experience-based tuning to maintain performance across the flight envelope. The proposed method combines LADRC with adaptive multi-objective optimization: the LESO estimates and compensates for parameter perturbations and cross-coupling disturbances online, while the improved algorithm searches the prescribed domain for robust controller parameters to maintain attitude tracking and flight-safety margins.

2.3. Definition of the Near-Limit Attitude-Recovery Task Under Boundary Conditions

Engineering scenarios such as mountainous-area reconnaissance, emergency pull-up maneuvers, and valley gusts may force a UAV outside its conventional flight regime into an asymmetric aerodynamic region with strong disturbances, challenging controller disturbance rejection. To excite the model's strong aerodynamic coupling and evaluate attitude-controller robustness, this section defines a continuous multi-cycle near-limit attitude-recovery task. A continuous roll-command generation module is constructed for this task, as shown in Figure 3.

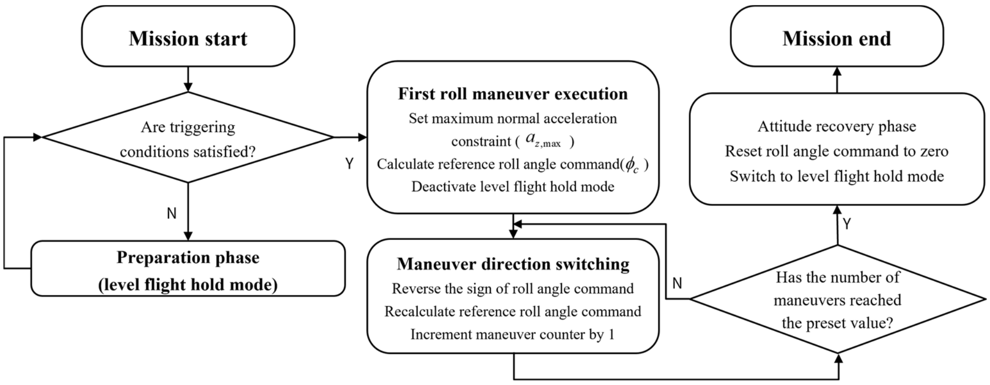

Figure 3. Roll-command execution logic.

The physical boundaries of the near-limit attitude-recovery test are specified. Airspeed is maintained near the right boundary of the flight envelope at approximately 150 m/s, and altitude is maintained within the high-altitude, low-density range of 5200~5700 m. Under these conditions, the dynamic pressure varies with altitude and external disturbances, aerodynamic damping decreases, and the risk of aircraft instability increases.

To satisfy the structural load limits of the airframe, the attitude command is no longer specified as a fixed-amplitude step signal. Instead, the roll-angle reference is dynamically calculated according to the maximum allowable normal acceleration, as defined by

$$\phi_c = turn\_right \times \operatorname{acos}(g / a_{z,\max}) \tag{9}$$

where ϕ_c is the dynamic roll-angle command calculated according to the normal-load constraint; $turn\_right$ is the turning-direction indicator, with a positive value representing recovery toward the right and a negative value representing recovery toward the left; $a_{z,\max}$ denotes the magnitude of the maximum allowable normal acceleration of the airframe, in $\mathrm{m/s^2}$; and $n_{z,\max}$ denotes the corresponding maximum allowable normal load factor, which is dimensionless. They are related by $n_{z,\max} = a_{z,\max} / g$, $a_{z,\max} = n_{z,\max} g$.

During task execution, the system alternates the direction indicator $turn\_right$ and cyclically generates roll commands in opposite directions, producing continuous alternating disturbances. After the prescribed number of maneuvers has been completed, the command smoothly returns to zero, and the normal-acceleration command returns to its reference value of $a_{z,c} = -9.8\ \text{m/s}^2$. From the perspective of the underlying dynamic mechanism, continuous large-angle maneuvers generate coupling between the lateral and longitudinal moments, increasing the generalized total disturbance of the system. This effect is further compounded by the nonlinear degradation of control effectiveness at high altitudes. The proposed test can reveal the performance limitations of fixed-parameter controllers under boundary conditions and provides an engineering-relevant verification benchmark for the parameter tuning of the multi-objective optimization algorithm presented subsequently.

3. Control Architecture and Multi-Objective Optimization Algorithm

To address the strong nonlinear coupling and large aerodynamic parameter perturbations under the boundary conditions described above, while considering the constraints imposed by the near-limit attitude-recovery task in Section 2.3, this section adopts a cascaded architecture with attitude and load-factor stability augmentation in the outer loop and angular-rate stability augmentation in the inner loop across all three axes. To address the difficulty of manually tuning multichannel LADRC parameters and balancing performance over the full flight envelope, an improved NSGA-II integrating hierarchical pre-optimization and a threefold adaptive mechanism is designed. Independent channel-by-channel optimization and coordinated full-envelope parameter scheduling are combined to systematically tune the three-channel controller.

3.1. Design of the Attitude and Load-Factor Stability-Augmentation Loop

To match the six-degrees-of-freedom nonlinear model, an outer attitude and load-factor stability-augmentation system (hereinafter, the attitude stability-augmentation loop) is designed within a two-level cascaded architecture. The outer loop comprises an attitude-angle dynamic-inversion loop and a load-factor correction loop: dynamic inversion compensates for kinematic coupling during large-attitude maneuvers, while load-factor correction supports maneuver-load tracking. The pitch channel uses mode-dependent control, with pitch-angle control during level flight and small maneuvers and normal-load control during large-bank roll maneuvers. The roll channel uses dynamic inversion throughout for roll-angle tracking, while the yaw channel uses lateral-load control to attenuate lateral–directional coupling disturbances. LADRC is applied in all angular-rate stability-augmentation loops for angular-rate tracking and disturbance rejection. The outer-loop control laws are derived below.

3.1.1. Pitch-Angle Control Loop of the Pitch Channel

To accommodate flight conditions across the tested envelope, the pitch-channel attitude stability-augmentation loop uses mode-dependent control. During level flight and small-amplitude maneuvers, pitch angle is the control objective. A dynamic-inversion controller is designed from the kinematic relationship in Equation (3) to reduce the effects of model errors and bounded external disturbances and support attitude tracking. The pitch-angle kinematic relationship is

$$\dot{\theta} = q\cos\phi - r\sin\phi \tag{10}$$

A proportional control structure is employed for pitch-angle control, and the desired pitch-angle rate is designed as $\dot{\theta} = k_\theta\left(\theta_c - \theta\right)$, where k_θ denotes the bandwidth of the pitch-angle control loop and θ_c denotes the pitch-angle command. By combining

Equation (10) with the proportional control law and compensating for the roll-angle coupling term, the commanded pitch angular rate is derived as

$$q_c = (k_\theta(\theta_c - \theta) + r\sin\phi)/\cos\phi \tag{11}$$

where q_c is the pitch angular rate command generated by the pitch-angle control loop and serves as the control input to the LADRC-based angular-rate stability-augmentation loop (hereinafter, the angular-rate LADRC).

3.1.2. Normal-Load Stability-Augmentation Loop of the Pitch Channel

During large-roll maneuvers, cross-coupling among the three rotational axes increases, and a single pitch-angle closed loop cannot simultaneously satisfy normal-load tracking and dynamic-response requirements. A normal-load stability-augmentation loop is therefore designed, as shown in Figure 4.

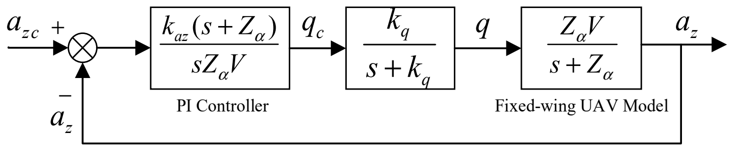

Figure 4. Block diagram of the normal-load control structure.

The normal-load controller adopts a proportional–integral (PI) correction structure and outputs a pitch angular rate command to the angular-rate stability-augmentation loop. The controller parameters are dynamically adjusted according to the dynamic pressure. Under the longitudinal small-disturbance assumption, the pitch angle θ, angle of attack α, and flight-path angle γ satisfy the geometric relationship $\theta = \alpha + \gamma$. Differentiating this relationship with respect to time and combining it with the relationship between the normal acceleration and flight-path angle, $V\dot{\gamma} = a_z$, yields $\dot{\theta} = \dot{\alpha} + a_z / V$. When lateral–directional coupling effects are neglected, $\dot{\theta} \approx q$. According to the aerodynamic relationship between the normal acceleration and angle of attack, $a_z = \bar{q}SC_{L\alpha}\alpha / m$, the normal-force derivative is defined as $Z_\alpha = \bar{q}SC_{L\alpha}/(mV)$. The transfer function from the pitch angular rate to the normal acceleration can then be derived as

$$a_z(s)/q(s) = Z_\alpha V/(s+Z_\alpha) \tag{12}$$

Since the angular-rate stability-augmentation loop has a faster response, the dynamics from the angular-rate command to the actual angular rate can be approximated by the first-order inertial element $q(s)/q_c(s) = k_q/(s+k_q)$, where k_q denotes the control bandwidth of the pitch angular rate stability-augmentation loop. Combining Equation (12) with this first-order element gives the overall transfer function. The system contains two poles, $-k_q$ and $-Z_\alpha$, of which $-Z_\alpha$ lies close to the imaginary axis. To optimize the dynamic characteristics of the system, a PI controller is designed to cancel the pole $-Z_\alpha$, while an integral term is introduced to eliminate the steady-state error. The resulting control law of the normal-load stability-augmentation loop is

$$q_c = \frac{s+Z_\alpha}{sZ_\alpha V}k_{az}(a_{zc} - a_z) = \frac{k_{az}(a_{zc} - a_z)}{Z_\alpha V}\left(1 + \frac{Z_\alpha}{s}\right) \tag{13}$$

where a_{zc} denotes the normal-acceleration command and k_{az} denotes the normal-load control gain. After pole cancelation, the characteristic equation of the closed-loop normal-load system is $s^2 + k_q s + k_{az}k_q = 0$. With the damping ratio set to the commonly used engineering value $\zeta = 0.707$, the normal-load loop gain and angular-rate loop bandwidth satisfy the tuning relationship $k_{az} = k_q / (2\zeta)^2$, where k_q is the pitch angular rate loop bandwidth.

3.1.3. Roll-Angle Control Loop of the Roll Channel

The roll-angle loop adopts the same dynamic-inversion architecture as the pitch-angle loop. The command is calculated from the roll-channel kinematic equation to reduce the effects of model uncertainties and bounded external disturbances and eliminate kinematic coupling under large-attitude conditions. According to Equation (3), the roll-channel kinematic equation is

$$\dot{\phi} = p + \tan\theta(q\sin\phi + r\cos\phi) \tag{14}$$

A proportional control structure is adopted for roll-angle control, and the desired roll-angle rate is designed as $\dot{\phi} = k_\phi(\phi_c - \phi)$, where k_ϕ denotes the roll-angle control gain and ϕ_c denotes the roll-angle command. By combining Equation (14) with the proportional control law and compensating for the coupling terms involving the pitch angle and the three-axis angular rates, the roll-angular-rate command is derived as

$$p_c = k_\phi(\phi_c - \phi) - \tan\theta(q\sin\phi + r\cos\phi) \tag{15}$$

where p_c denotes the roll-angular-rate command and serves as the control input to the angular-rate LADRC.

3.1.4. Lateral-Load Stability-Augmentation Loop of the Yaw Channel

Consistent with the normal-load control architecture of the pitch channel, the yaw channel adopts a cascaded structure combining a lateral-load stability-augmentation loop with a yaw-angular-rate stability-augmentation loop. The lateral acceleration is selected as the control objective to satisfy the directional-stability requirements under boundary conditions. The lateral-force stability derivative is defined as $Z_\beta = -\rho V^2 S C_{Y\beta} / (2mV)$, and the control law of the lateral-load stability-augmentation loop is

$$r_c = k_{ay}(a_{yc} - a_y)\frac{s + Z_\beta}{V s Z_\beta} \tag{16}$$

where r_c denotes the yaw-angular-rate command, a_{yc} denotes the lateral-acceleration command, and k_{ay} denotes the lateral-load control gain. Following the same derivation as that for the normal-load loop of the pitch channel, the corresponding gain-tuning relationship is obtained as $k_{ay} = k_r / (2\zeta)^2$, where k_r denotes the control bandwidth of the yaw-angular-rate stability-augmentation loop, and the damping ratio is assigned the commonly used engineering value $\zeta = 0.707$.

3.2. Design of the Three-Channel LADRC Angular-Rate Stability-Augmentation Loops

This section combines a general derivation with channel-specific design. First, a general three-channel LADRC framework is established, and each channel's control plant is reconstructed into a standard form. The general LESO structure and stability analysis are then presented. Finally, channel-specific LSEF control laws are derived using subscripts, preserving the common method while accounting for differences in channel aerodynamics.

3.2.1. Reconstruction of the Three-Channel Control Plants

The core idea of LADRC is to treat aerodynamic coupling, parameter perturbations, and external disturbances in each channel as a generalized total disturbance and

https://doi.org/10.3390/drones10070532

reconstruct the nonlinear model into a standard integrator-chain form. The general angular-rate control plant is

$$\dot{x}_1 = f + b_0 u \tag{17}$$

where x_1 is the output corresponding to the angular rate of each channel; f is the generalized total disturbance, including nonlinear coupling, model uncertainties, and external disturbances; b_0 is the nominal control gain; and u is the control input corresponding to the control-surface deflection command.

Based on this general framework, the control plants of the three channels are reconstructed separately [28]. The subscripts q, p, and r are used to distinguish the pitch, roll, and yaw channels, respectively. The aerodynamic moments of the respective channels are calculated using Equation (4) and are therefore not repeated here.

(1) Reconstruction of the Pitch-Channel Control Plant

According to the rigid-body rotational Euler equation about the body-fixed y axis, the pitch angular rate dynamics are given by

$$\dot{q} = (M - pr(I_x - I_z)) / I_y \tag{18}$$

The nominal control gain is defined as $b_{q0} = M_{\delta_e} = C_{m\delta_e}\bar{q}S\bar{c} / I_y$. Substituting the aerodynamic pitching moment into the angular-rate dynamic equation and rearranging the resulting expression separates the dynamics into a disturbance term and a control term:

$$\dot{q} = \frac{\bar{q}S\bar{c}C_m + (\bar{q}/2V)S\bar{c}^2(C_{mq}q + C_{m\dot{\alpha}}\dot{\alpha}) - pr(I_x - I_z)}{I_y} + b_{q0}\delta_e \tag{19}$$

The kinematic cross-coupling terms, aerodynamic damping terms, interchannel coupling terms, model perturbations, and external disturbances are collectively treated as the generalized total disturbance x_{q2}. The pitch channel can then be reconstructed into the following standard second-order extended-state form:

$$\begin{cases} \dot{x}_{q1} = x_{q2} + b_{q0}u_q \\ \dot{x}_{q2} = g_q \end{cases} \tag{20}$$

where $u_q = \delta_e$ is the elevator control input, and $g_q = \dot{x}_{q2}$ is the rate of change in the total disturbance, which is assumed to be physically bounded.

(2) Reconstruction of the Roll- and Yaw-Channel Control Plants

The roll and yaw channels are reconstructed using the same procedure as that applied to the pitch channel. Let $x_{p1} = p$ and $x_{r1} = r$, with the corresponding control inputs defined as $u_p = \delta_a$ and $u_r = \delta_r$, respectively. The nominal control gains associated with the aileron and rudder are defined as $b_{p0} = L_{\delta_a} = C_{l\delta_a}\bar{q}Sb / I_x$, $b_{r0} = N_{\delta_r} = C_{n\delta_r}\bar{q}Sb / I_z$.

Substituting the aerodynamic rolling and yawing moments into the corresponding angular-rate dynamic equations and separating the control-surface terms yields:

$$\begin{cases} \dot{p} = \dfrac{\bar{q}SbC_l + (\bar{q}/2V)Sb^2(C_{lp}p + C_{lr}r) - qr(I_z - I_y)}{I_x} + b_{p0}\delta_a \\ \dot{r} = \dfrac{\bar{q}SbC_n + (\bar{q}/2V)Sb^2(C_{np}p + C_{nr}r) - pq(I_y - I_x)}{I_z} + b_{r0}\delta_r \end{cases} \tag{21}$$

The nonlinear aerodynamic terms, inertial coupling terms, parameter perturbations, and external disturbances in the two channels are collectively defined as the generalized total disturbances x_{p2} and x_{r2}, respectively. The roll- and yaw-channel control plants can therefore be reconstructed as

$$\begin{cases}\dot{x}_{p1} = x_{p2} + b_{p0}u_p \\ \dot{x}_{p2} = g_p\end{cases} \quad \begin{cases}\dot{x}_{r1} = x_{r2} + b_{r0}u_r \\ \dot{x}_{r2} = g_r\end{cases} \tag{22}$$

where $u_p = \delta_a$ and $u_r = \delta_r$ denote the aileron and rudder control inputs, respectively, while $g_p = \dot{x}_{p2}$ and $g_r = \dot{x}_{r2}$ denote the rates of change in the generalized total disturbances in the roll and yaw channels. For the three channels, g_q, g_p, and g_r are assumed to remain bounded within the considered flight envelope.

3.2.2. General LESO Design

For the reconstructed integrator-chain control plants, a second-order linear extended state observer (LESO) is designed for all three channels [0,29] to avoid the gain chattering that may occur in conventional nonlinear observers under high-frequency disturbances. The LESO simultaneously estimates the three-axis angular rates and generalized total disturbances online:

$$e_1 = z_1 - y,\ \dot{z}_1 = z_2 + b_0 u - \beta_1 e_1,\ \dot{z}_2 = -\beta_2 e_1 \tag{23}$$

where e_1 denotes the state observation error; z_1 and z_2 denote the estimated angular rate and generalized total disturbance, respectively; and β_1 and β_2 are the linear gain parameters of the LESO. For channel-specific implementation, only the corresponding subscripted physical variables need to be substituted, while the observer structure and parameter-configuration rules remain identical.

3.2.3. Stability Proof of the General LESO

Define the general system observation errors as $e_1 = z_1 - x_1$ and $e_2 = z_2 - x_2$. Assume that the rate of change in the total disturbance is $\dot{x}_2(t) = g(t)$ and is bounded in the physical system, i.e., $|g(t)| \le g_0$. Subtracting Equation (17) from Equation (23) yields the following observation-error dynamics [29]:

$$\dot{e}_1 = -\beta_1 e_1 + e_2,\ \dot{e}_2 = -\beta_2 e_1 - g(t) \tag{24}$$

A coordinate transformation is introduced by defining the new state variables $X_1 = e_1(t)$ and $X_2 = e_2 - \beta_1 e_1$. The error dynamics can then be rewritten as $\dot{X}_1 = X_2$ and $\dot{X}_2 = -\beta_2 e_1 - g(t) - \beta_1 X_2$. Consider the following positive-definite Lyapunov function: $V(t) = \beta_2 X_1^2/2 + X_2^2/2$. Differentiating $V(t)$ with respect to time yields

$$\dot{V}(t) = \beta_2 e_1 X_2 + X_2(-\beta_2 e_1 - g(t) - \beta_1 X_2) = -X_2(g(t) + \beta_1 X_2) \tag{25}$$

Under the ideal condition of a constant disturbance, i.e., $g(t) = 0$, the Lyapunov derivative becomes $\dot{V}(t) = -\beta_1 X_2^2 < 0$, indicating asymptotic stability. For a dynamically varying but bounded disturbance, $\dot{V}(t) < 0$ holds, provided that $X_2\left(g(t) + \beta_1 X_2\right) > 0$. Thus, the observation-error states ultimately converge to the steady-state bounds $|e_1| \le g_0/\beta_2$ and $|e_2| \le \beta_1 g_0/\beta_2$. Accordingly, when the observer gains are appropriately configured using bandwidth parameterization and increased such that $\beta_2 \gg g_0$, the steady-state tracking error of the LESO can be reduced and remain ultimately bounded, indicating convergent behavior.

3.2.4. Three-Channel LSEF Outputs

For the reconstructed standard integrator-chain model of each channel, a linear state error feedback (LSEF) control law is designed to achieve angular-rate tracking and disturbance compensation. In channel-specific applications, the general variables need only be replaced with the corresponding subscripted physical quantities, while the control structure remains universal. The pitch channel is used below as an example to derive the LSEF output.

Based on the angular-rate and total-disturbance estimates generated by the general LESO, a closed-loop pitch angular rate controller is constructed using proportional feedback and total-disturbance feedforward compensation [29]. First, a nominal virtual control law without disturbance compensation is constructed from the angular-rate tracking error, $u_{q0} = k_q\left(q_c - z_{q1}\right)$, which achieves command tracking. In steady state, the estimated angular rate converges to the actual angular rate; therefore, the measured angular rate may be used directly in implementation.

The total-disturbance estimate z_{q2} is introduced for feedforward compensation to cancel the generalized total disturbance and transform the system into a standard integrator-chain form. Separating the nominal control term gives the elevator-deflection command:

$$\delta_e = \frac{u_{q0} - z_{q2}}{b_{q0}} = \frac{k_q(q_c - q) - z_{q2}}{b_{q0}} \tag{26}$$

where q_c denotes the pitch angular rate command generated by the dynamic-inversion component of the attitude stability-augmentation loop, and k_q denotes the pitch angular rate closed-loop control gain, which determines the closed-loop bandwidth of the system.

Similarly, the LSEF control laws for the roll and yaw channels are, respectively, given by

$$\begin{cases} \delta_a = \dfrac{u_{p0} - z_{p2}}{b_{p0}} = \dfrac{k_p(p_c - p) - z_{p2}}{b_{p0}} \\ \delta_r = \dfrac{u_{r0} - z_{r2}}{b_{r0}} = \dfrac{k_r(r_c - r) - z_{r2}}{b_{r0}} \end{cases} \tag{27}$$

where p_c and r_c denote the roll- and yaw-angular-rate commands, respectively; k_p and k_r are the corresponding closed-loop control gains.

The pitch-channel LADRC architecture is shown in Figure 5. The basic ADRC framework follows classical ADRC theory [0], and the control architecture is based on [29].

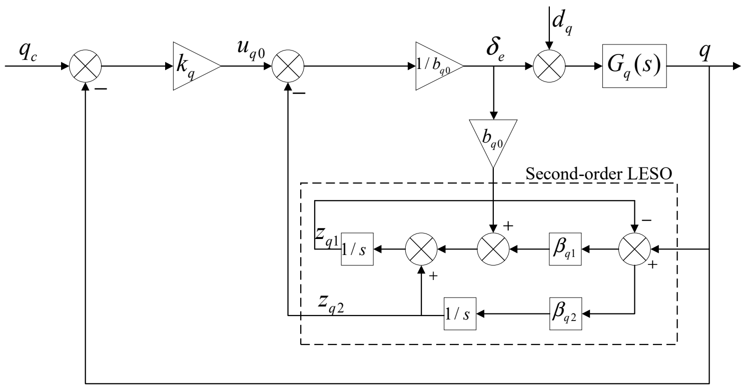

Figure 5. Architecture of the pitch-channel LADRC controller.

3.2.5. LESO Gain-Configuration Criteria and Sensitivity Analysis

The bandwidth method is used to configure the second-order LESO gains, and bandwidth-selection and sensitivity criteria are provided for the three attitude channels.

(1) Bandwidth-Based Gain Configuration

According to the error dynamics in Equation (24), the characteristic equation of the LESO is $s^2 + \beta_1 s + \beta_2 = 0$. Placing both observer poles at $-\omega_o$ gives $(s+\omega_o)^2 = s^2 + 2\omega_o s + \omega_o^2 = 0$. By comparing the coefficients,

$$\beta_1 = 2\omega_o,\ \beta_2 = \omega_o^2 \tag{28}$$

where ω_o denotes the observer bandwidth in rad/s. Once ω_o is specified, the corresponding LESO gains for the roll, pitch, and yaw channels are determined.

(2) Engineering Criteria for Observer-Bandwidth Selection

(a) Bandwidth matching: Because LESO tracking speed and estimation behavior depend strongly on observer bandwidth [30], the initial observer-bandwidth range for the tested platform is set as $\omega_o = (3 \sim 10)\omega_c$, where ω_c denotes the closed-loop angular-rate bandwidth of the corresponding channel. The range is subsequently refined for the tested UAV through preliminary simulations and optimization to balance estimation speed, noise sensitivity, and unmodeled dynamics.

(b) Performance trade-off: Increasing ω_o accelerates disturbance estimation but also increases high-frequency-noise amplification. For the tested platform, an initial ratio of $5 \sim 8$ is used in low-noise simulations, whereas a ratio of $3 \sim 5$ is used when sensor-noise sensitivity is emphasized; the final value is determined by optimization.

(c) Platform-specific initialization: For the angular-rate stabilization loops considered here, ω_o is initialized within $10 \sim 50$ rad/s and adjusted with altitude, airspeed, and dynamic pressure during the platform-specific tuning process.

(3) Gain-Parameter Sensitivity Analysis

(a) Tracking performance: Within an appropriate range, increasing ω_o reduces the observation error over the tested tuning range. When ω_o approaches the upper part of the platform-specific range ($10\omega_c$), the additional improvement becomes limited while noise sensitivity increases.

(b) Noise characteristics: Increasing the observer gains is positively correlated with noise amplification, and β_2 is much more sensitive to noise than β_1. The upper bandwidth limit should thus be selected according to the sensor-noise level.

(c) Stability: Under the ideal continuous-time error model, the characteristic roots lie in the left half-plane when $\omega_o > 0$. However, excessive bandwidth may interact with actuator delays and unmodeled high-frequency dynamics, inducing limit-cycle oscillations. Frequency-domain analysis should therefore ensure that ω_o remains below the cutoff frequency of the unmodeled dynamics.

3.3. Multi-Objective Optimization Evaluation Index System

3.3.1. Multi-Objective Optimization Indices

For the near-envelope attitude-recovery task considered in this study, the authors formulate four complementary optimization indices to represent altitude safety, airspeed retention, roll tracking, and steady-state smoothness. The first three use standard maximum-error or RMSE forms, whereas the fourth is a task-specific steady-state roll-oscillation measure. Together, they capture the nonlinear and multivariable coupling that cannot be represented by a single error metric.

(1) Maximum Altitude Deviation J_1: During a large-bank maneuver, the inclined lift vector reduces the vertical lift component, while lateral–longitudinal coupling may result in altitude loss. To evaluate the control stability of the vertical envelope, the maximum absolute deviation between the actual and desired altitudes during the task is defined as

$$J_1 = \max_{t \in [t_s, t_e]} | h(t) - h_d | \tag{29}$$

where $h(t)$ and h_d denote the actual altitude and desired level-flight altitude, respectively, while t_s and t_e denote the start and end times of the task. A smaller J_1 indicates a smaller maximum altitude deviation during the task.

(2) Airspeed-Tracking RMSE J_2 : The additional drag generated during large maneuvers may cause airspeed variations, reduce sustained maneuverability, and alter the aerodynamic damping associated with dynamic pressure. The root mean square error (RMSE) between the actual and desired airspeeds is used to evaluate airspeed retention and energy-matching performance:

$$J_2 = \sqrt{\frac{1}{N} \sum_{k=1}^{N} [V(k) - V_d(k)]^2} \tag{30}$$

where $V(k)$ and $V_d(k)$ denote the actual and desired airspeeds at the k-th sampling instant, respectively, and N is the total number of sampling points during the task.

(3) Roll-Tracking RMSE J_3 : After the altitude and airspeed constraints are considered, the RMSE between the actual and commanded roll angles is used to evaluate the tracking performance of the controller:

$$J_3 = \sqrt{\frac{1}{N} \sum_{k=1}^{N} [\phi(k) - \phi_d(k)]^2} \times 57.3 \tag{31}$$

where $\phi(k)$ and $\phi_d(k)$ denote the actual and commanded roll angles, respectively. The factor 57.3 converts the angular error from radians to degrees.

(4) Roll-Oscillation Index J_4 : High feedback gains may intensify structural oscillations and cause high-frequency actuator saturation. To evaluate steady-state smoothness, only the steady-state segment of the roll response is considered, thereby excluding the monotonic variation during the transient stage. The index is defined as the root mean square deviation of the roll angle from its steady-state mean:

$$J_4 = \sqrt{\frac{1}{k_e - k_s + 1} \sum_{k=k_s}^{k_e} [\phi(k) - \bar{\phi}]^2} \tag{32}$$

where k_s and k_e denote the initial and final sampling points of the selected steady-state segment, respectively, and $\bar{\phi}$ is the mean roll angle over this interval. A smaller J_4 indicates weaker steady-state oscillation and smoother attitude response, with lower structural-load impact from high gains.

In summary, $J_1 - J_4$ characterize altitude safety, airspeed retention, roll tracking, and steady-state smoothness, respectively, and constitute a set of mutually constraining and complementary multi-objective optimization criteria.

3.3.2. Auxiliary Roll-Response Comparison Indices

Seven auxiliary indices are used only for the before-and-after comparison of the roll-angle response and are distinct from the four optimization objectives $J_1 - J_4$. These indices are defined as follows.

(1) Rise time t_r: The time required for the roll-angle response to rise from 10% to 90% of the step amplitude, reflecting the response speed. It is calculated as:

$$t_r = t_{90\%} - t_{10\%} \tag{33}$$

where $t_{10\%}$ and $t_{90\%}$ are the first times at which the response reaches 10% and 90% of the step amplitude, respectively.

(2) Percentage overshoot $\sigma\%$: The percentage by which the response peak exceeds the steady-state command magnitude, reflecting response smoothness. It is calculated as:

$$\sigma\% = (|\phi_{peak}| - |\phi_{c,steady}|)/|\phi_{c,steady}| \times 100\% \quad (34)$$

where ϕ_{peak} is the peak roll angle within the step-response window, and $\phi_{c,\text{steady}}$ is the steady-state amplitude of the roll-angle command.

(3) Settling time t_s: The minimum time after which the response enters and remains within the $\pm 5\%$ error band of the steady-state command magnitude, reflecting the convergence speed. It is calculated as:

$$t_s = \min\{t \mid \forall t' \geq t,\ ||\phi(t')| - |\phi_{c,steady}|| \leq 0.05|\phi_{c,steady}|\} \quad (35)$$

where $\phi(t')$ is the actual roll angle at time t', and $0.05|\phi_{c,\text{steady}}|$ is the threshold of the 5% error band.

(4) Steady-state error e_{steady}: The mean absolute deviation between the actual and commanded roll angles over the steady-state segment, reflecting steady-state tracking accuracy. It is calculated as:

$$e_{steady} = \frac{1}{M}\sum_{i=N-M+1}^{N} |\phi(i) - \phi_c(i)| \quad (36)$$

where $\phi(i)$ and $\phi_c(i)$ are the actual and commanded roll angles at the i-th sampling instant, respectively; N is the total number of sampling points; and M is the number of sampling points in the steady-state segment.

(5) RMS tracking error: The root mean square error between the actual and commanded roll angles over the entire evaluation interval, reflecting overall tracking accuracy. It is calculated as:

$$RMS = \sqrt{\frac{1}{N}\sum_{i=1}^{N}(\phi(i) - \phi_c(i))^2} \quad (37)$$

where $\phi(i)$ and $\phi_c(i)$ are the actual and commanded roll angles at the i-th sampling instant, respectively, and N is the total number of sampling points.

(6) Integral absolute error IAE: The time integral of the absolute difference between the actual and commanded roll angles over the evaluation interval. It is calculated as:

$$\text{IAE} = \sum_{i=1}^{N} |\phi(i) - \phi_c(i)|\Delta t \quad (38)$$

where $\phi(i)$ and $\phi_c(i)$ are the actual and commanded roll angles at the i-th sampling instant, respectively; N is the total number of sampling points; and Δt is the sampling time step.

(7) Control energy E_c: The time integral of the squared roll-angle rate, used as an approximate measure of control effort. It is calculated as:

$$E_c = \sum_{i=1}^{N}\left(\frac{d\phi}{dt}(i)\right)^2 \Delta t \quad (39)$$

where $d\phi/dt(i)$ is the roll-angle rate at the i-th sampling instant, and Δt is the sampling time step.

3.3.3. Algorithm-Comparison Metrics

Four metrics compare optimization algorithms: final convergence value, relative improvement rate, convergence generation, and post-convergence coefficient of variation.

(1) Final convergence value J_{final}: the mean of each objective over generations 51–60 is first calculated and then combined using the initial objective weights:

$$j_n = \frac{1}{10}\sum_{t=51}^{60} \text{avg\_fit}_n(t),\ \ J_{final} = \sum_{n=1}^{4} w_{\text{base},n} j_n, \quad (40)$$

where $\mathrm{avg\_fit}_n(t)$ denotes the mean fitness of the n-th objective at generation t, $w_{\mathrm{base},n}$ is its initial weight, and $n = 1,2,3,4$. A smaller J_{final} indicates a better overall optimization result over the final 10 generations.

(2) Relative improvement rate η: this metric measures the reduction in the final convergence value relative to the benchmark algorithm:

$$\eta = (J_{base,final} - J_{alg,final}) / J_{base,final} \times 100\%, \tag{41}$$

where $J_{\mathrm{base,final}}$ and $J_{\mathrm{alg,final}}$ denote the final convergence values of the benchmark and evaluated algorithms, respectively. A larger η indicates a greater relative reduction in comprehensive fitness.

(3) Number of generations to convergence t_{conv}: a threshold 2% above the final mean fitness of each objective is used:

$$t_n = \min\{t \mid \mathrm{avg\_fit}_n(t) \le 1.02 j_n\}, \quad t_{\mathrm{conv}} = \max_{n=1,2,3,4}\{t_n\}, \tag{42}$$

where t_n is the first generation at which the n-th objective reaches its threshold. The overall convergence generation is determined by the last of the four objectives to reach its corresponding threshold, and a smaller value indicates faster convergence.

(4) Coefficient of variation after convergence CV: this metric uses the same post-convergence interval for all four objectives:

$$\begin{cases} \sigma_n = \mathrm{std}(\{\mathrm{avg\_fit}_n(t)\}_{t=t_{\mathrm{conv}}}^{60}), \\ CV_n = \sigma_n / \mathrm{mean}(\{\mathrm{avg\_fit}_n(t)\}_{t=t_{\mathrm{conv}}}^{60}), \quad CV = \dfrac{1}{4}\displaystyle\sum_{n=1}^{4} CV_n, \end{cases} \tag{43}$$

where $\mathrm{mean}(\cdot)$ and $\mathrm{std}(\cdot)$ denote the mean and standard deviation, respectively. A smaller CV indicates lower relative fluctuation during the post-convergence stage.

3.4. Optimization Variables and Baseline NSGA-II Procedure

After establishing the multi-objective evaluation system, the high-dimensional parameter space under conflicting physical constraints must be searched efficiently. NSGA-II with elitist preservation is adopted. Its Pareto-ranking process does not require predefined objective weights; fast non-dominated sorting and crowding distance are used to generate a well-distributed Pareto solution set in the nonlinear parameter space and coordinate control response, disturbance rejection, and flight safety. The parameter mapping and iterative procedure are presented below.

3.4.1. Gain-Scheduling Decision Variables

The LADRC angular-rate stabilization loop is jointly determined by the proportional gain k_i and the observer gains β_{i1} and β_{i2}. Under near-envelope conditions, the dynamic pressure varies with airspeed. A fixed-gain controller may provide insufficient control effectiveness at low dynamic pressure and induce high-frequency aerodynamic divergence at high dynamic pressure. Each gain is therefore linearly scheduled with dynamic pressure using a slope and an intercept, resulting in six optimization variables for each channel:

$$k_i = \bar{q}k_{ik} + b_{ik}, \quad \beta_{i1} = \bar{q}k_{i\beta 1} + b_{i\beta 1}, \quad \beta_{i2} = \bar{q}k_{i\beta 2} + b_{i\beta 2} \tag{44}$$

where $\bar{q}$ denotes the real-time dynamic pressure; k_{ij} and b_{ij} are the scheduling slope and intercept of the corresponding gain, respectively; $i \in \{p,q,r\}$ denotes the roll, pitch, and yaw channels; and $j \in \{k, \beta_1, \beta_2\}$ identifies the gain type.

Each channel contains three dynamic-pressure-scheduled LADRC gains: one control gain and two observer gains. Each gain is represented by a slope and an intercept, giving six decision coefficients per channel. Across the roll, pitch, and yaw channels, this corresponds to nine gain-scheduling functions and 18 coefficients. Because the channels are optimized sequentially, each optimization run remains six-dimensional. The four objectives $J_1 - J_4$ and the seven auxiliary response indices are performance measures rather than scheduling variables. Table 2 gives the coefficient bounds and physical meanings.

Table 2. Search bounds for the scheduled LADRC gain coefficients in the three channels.

Control Channel	Scheduled Gain Coefficients	Lower Bound	Upper Bound	Physical Interpretation
Roll channel	k_{pk}, b_{pk}	10^{-5}, -5	10^{-3}, 5	Slope and intercept of the control gain
	$k_{p\beta1}$, $b_{p\beta1}$	10^{-5}, -5	10^{-3}, 5	Slope and intercept of the observer gain β_1
	$k_{p\beta2}$, $b_{p\beta2}$	5×10^{-4}, -10	1.5×10^{-3}, 10	Slope and intercept of the observer gain β_2
Pitch channel	k_{qk}, b_{qk}	10^{-5}, -5	10^{-3}, 5	Slope and intercept of the control gain
	$k_{q\beta1}$, $b_{q\beta1}$	10^{-5}, -5	10^{-3}, 5	Slope and intercept of the observer gain β_1
	$k_{q\beta2}$, $b_{q\beta2}$	5×10^{-4}, -10	1.5×10^{-3}, 10	Slope and intercept of the observer gain β_2
Yaw channel	k_{rk}, b_{rk}	10^{-5}, -5	10^{-3}, 5	Slope and intercept of the control gain
	$k_{r\beta1}$, $b_{r\beta1}$	10^{-5}, -5	10^{-3}, 5	Slope and intercept of the observer gain β_1
	$k_{r\beta2}$, $b_{r\beta2}$	5×10^{-4}, -10	1.5×10^{-3}, 10	Slope and intercept of the observer gain β_2

Note: Each scheduled gain is represented by one slope and one intercept. Thus, each channel has six decision coefficients; the three channels contain nine gain-scheduling functions and 18 coefficients in total.

3.4.2. Baseline NSGA-II Evolution

After the decision space and evaluation indices have been established, a hierarchical selection mechanism is employed to guide the population toward the Pareto front. The specific iterative procedure is described below.

(1) Population Initialization and Encoding

A random initial population is generated and binary encoding is used. Each single-channel LADRC contains six parameters to be optimized, and each parameter is represented by a gene segment with an encoding length of $l = 9$. The physical parameter is mapped to a binary-coded integer as

$$X = \mathrm{int}\left[\frac{x - U_{\min}}{U_{\max} - U_{\min}} \bullet \left(2^l - 1\right)\right] \tag{45}$$

where x is the physical value of the parameter, $U_{\min}$ and $U_{\max}$ are its lower and upper bounds, and X is the corresponding coded integer.

(2) Fast Non-Dominated Sorting and Hierarchical Selection

For an individual x^*, if another individual x satisfies $fit_i(x) \le fit_i(x^*),\ (i = 1,2,3,4)$ for all objectives, with a strict inequality for at least one objective, then x dominates x^*. If no such individual exists, x^* is regarded as a non-dominated solution in the current population. The population is subsequently divided into non-dominated fronts, and individuals in fronts with higher selection priority are retained first, thereby enabling the four conflicting objectives to be considered simultaneously.

(3) Crowding-Distance Calculation for Maintaining Population Diversity

Crowding distance measures the local distribution density of individuals within the same non-dominated front. When two individuals belong to the same front, the individual with the larger crowding distance is preferred to maintain the distribution range of the Pareto solution set:

$$d_i = \sum_{r=1}^{4} \frac{fit_r(x_{i+1}) - fit_r(x_{i-1})}{fit_{r,max} - fit_{r,min}} \tag{46}$$

where d_i denotes the crowding distance of the i-th individual; x_{i-1} and x_{i+1} are its adjacent individuals after sorting according to the r-th objective; and $fit_{r,\max}$ and $fit_{r,\min}$ are the maximum and minimum values of the r-th objective within the corresponding front.

(4) Genetic Strategy and Comprehensive Fitness Evaluation

Elite individual selection iterates through each front from highest to lowest priority, selecting half of the population as evolutionary parents, while the remaining individuals form the unselected set to receive new genes generated by crossover and mutation. To evaluate the overall performance of elite individuals, the base-weight vector is defined as

$$W_{\text{base}} = \left[w_h, w_v, w_\phi, w_o \right] = \left[100, 10, 1000, 100 \right] \tag{47}$$

where w_h, w_v, w_ϕ, and w_o correspond to $J_1 - J_4$, respectively. These weights are used only for the comprehensive evaluation of elite individuals and do not replace the non-dominated sorting of NSGA-II. The comprehensive fitness of the i-th individual is calculated as

$$Cphfit_i = \sum_{r=1}^{4} fit_r(x_i) \times w_r \tag{48}$$

where $fit_r(x_i)$ denotes the fitness of the individual x_i for the r-th objective, and w_r is the corresponding weight.

(5) Crossover and Mutation Operations

The algorithm switches between adjacent-elite crossover and tournament-selection crossover according to the comprehensive fitness state of the population. Adjacent-elite crossover is used when the comprehensive fitness is relatively large, whereas tournament-selection crossover is used when it is relatively small. During mutation, a position is randomly selected within the 9-bit gene segment of each parameter, and its binary value is inverted to preserve search diversity in the parameter space.

3.5. Hierarchical Adaptive NSGA-II Procedure

The proposed algorithm is presented using an input–stage–output structure. Its inputs are the LADRC parameter bounds, population size, generation limits, and initial objective weights. Stage I generates objective-specialized initial individuals through four parallel single-objective searches; Stage II performs multi-objective evolution with adaptive parameter ranges, crossover/mutation probabilities, and objective weights. The output is the Pareto-optimal LADRC parameter set, and Figure 6 summarize the overall workflow of the proposed hierarchical-adaptive NSGA-II procedure.

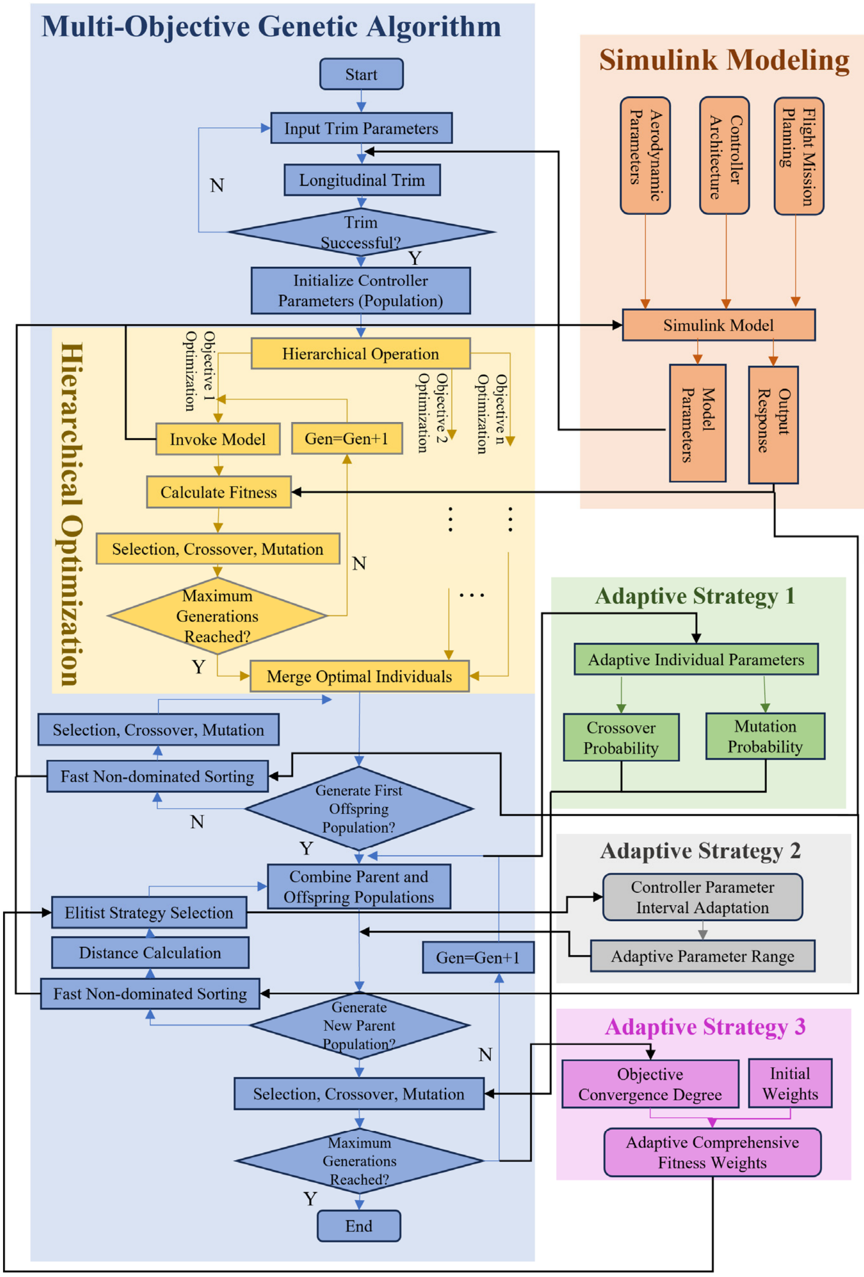

Figure 6. Two-stage workflow of the hierarchical adaptive NSGA-II.

3.5.1. Stage I: Hierarchical Single-Objective Pre-Optimization

Hierarchical pre-optimization follows a two-stage structure comprising single-objective preliminary searches and multi-objective coordinated optimization. The pre-optimized individuals perform better on individual objectives, placing the initial solution set closer to the non-dominated front boundary and increasing its crowding distance. This broadens the controller-parameter search range and supports convergence in the multi-objective stage.

The four subpopulations evolve in parallel, and their initial parameters are randomly generated within the physical constraints of the LADRC. Each subpopulation contains 20 individuals and is pre-optimized for ten generations. The single-objective fitness for the k-th objective is

$$f_k = \frac{1}{M}\sum_{m=1}^{M} e_{k,m} \tag{49}$$

where f_k is the fitness of the k-th objective, with $k=1,2,3,4$; M is the number of repeated simulations, set to $M=3$; and $e_{k,m}$ is the deviation of the k-th flight-performance criterion in the m-th simulation. Repeated simulations reduce the influence of stochastic wind-shear and aerodynamic disturbances on the evaluation, and the required flight states are obtained from the near-envelope nonlinear flight-dynamics model described in Section 2.2. After pre-optimization, the 10 individuals with the lower fitness values are selected from each subpopulation and merged to form 40 initial individuals for multi-objective optimization.

3.5.2. Stage II: Threefold Adaptive Multi-Objective Optimization

The threefold adaptive mechanism adjusts parameter-search ranges, genetic-operation probabilities, and objective-evaluation weights to coordinate exploration and local refinement and improve adaptation across the flight envelope. Adaptive parameter ranges update decision boundaries according to the elite distribution. Adaptive crossover and mutation probabilities regulate genetic intensity according to individual performance and parameter sensitivity. Adaptive objective weights modify the comprehensive evaluation according to the convergence stage of each objective. Their interaction with the dynamic-simulation evaluation is illustrated in Figure 6.

(1) Adaptive Parameter-Range Adjustment

This mechanism updates the search intervals of k_{ik}, $k_{i\beta 1}$, $k_{i\beta 2}$, b_{ik}, $b_{i\beta 1}$, and $b_{i\beta 2}$ according to the elite distribution in each generation. Initial physical bounds and a minimum-width constraint are imposed to prevent excessively wide intervals from reducing search efficiency and excessively narrow intervals from causing premature population concentration.

Step 1: Extract the parameter matrix of the elite individuals.

The physical values of all controller parameters are extracted from the elite-individual set S to construct the elite parameter matrix:

$$E=[p_{ij}]_{N\times 6} \tag{50}$$

where E denotes the extracted elite parameter matrix; N denotes the number of elite individuals; and p_{ij} denotes the value of the j-th parameter of the i-th elite individual. Here, $j=1,\ldots,6$ corresponds to the six parameters to be optimized for a single-channel LADRC controller. The six optimization parameters stored in the matrix correspond to the controller gain–dynamic-pressure mapping parameters in Equation (44). Their initial constraint ranges are determined according to the basic aerodynamic characteristics of the UAV and the LADRC stability boundaries.

Step 2: Calculate the actual distribution range of the elite parameters in each parameter dimension j:

$$m_j=\min_i p_{ij},\ M_j=\max_i p_{ij} \tag{51}$$

where m_j and M_j denote the actual lower and upper distribution bounds, respectively, of the j-th controller parameter in the current elite population.

Step 3: Determine the interval-expansion ratio according to the iteration progress.

The interval-expansion ratio λ is specified according to the normalized iteration progress $r=t/T$, where t denotes the current iteration number and T denotes the total number of iterations.

Step 4: Update the adaptive parameter ranges.

Taking the center of the elite parameter distribution as the reference, the interval is expanded outward by a prescribed proportion while ensuring that it does not exceed the initial physical constraint boundaries of the flight-control system:

$$L_j^{'} = \max\left(m_j - \left(M_j - m_j\right)\lambda, L_j^0\right),\ U_j^{'} = \min\left(M_j + \left(M_j - m_j\right)\lambda, U_j^0\right) \tag{52}$$

where $L_{j'}$ and $U_{j'}$ denote the updated adaptive lower and upper search bounds, respectively, while L_j^0 and U_j^0 denote the initial physical lower and upper constraint bounds of the j-th parameter, respectively.

Step 5: Enforce the minimum interval-width constraint.

To prevent the search space of the flight-control law from becoming fixed prematurely, the minimum parameter-range width is set to 20% of the initial interval width:

$$W_{\min} = 0.2 \times \left(U_j^0 - L_j^0\right) \tag{53}$$

If the current interval width satisfies $W_j = U_{j'} - L_{j'} < W_{\min}$, the interval is symmetrically expanded about its midpoint:

$$C_j = \left(U_j^{'} + L_j^{'}\right)/2,\ \ U_j^{'} = C_j + W_{\min}/2,\ \ L_j^{'} = C_j - W_{\min}/2 \tag{54}$$

where $W_{\min}$ denotes the minimum allowable search-width constraint and C_j denotes the midpoint of the current interval. If the minimum-width requirement still cannot be satisfied after symmetric expansion because of the initial physical boundaries, the interval is adjusted by fixing one side to the corresponding boundary and extending the other side until the required width is obtained.

Step 6: Update the parameter ranges of all individuals in the population.

The updated adaptive interval boundaries are applied to the entire population. The encoding step sizes are then recalculated, and all individuals are re-encoded accordingly.

(2) Adaptive Crossover and Mutation Probabilities

This mechanism allocates genetic-operation probabilities according to individual comprehensive fitness and parameter sensitivity. Better-performing individuals receive lower crossover and mutation probabilities for local refinement, whereas poorer-performing individuals receive higher probabilities for broader exploration. The probabilities of highly sensitive parameters are further reduced.

Let the population size be N, with each individual containing six parameters to be optimized. The following calculations are performed in each generation.

Step 1: Calculate the statistical quantities of the population's comprehensive fitness.

The comprehensive fitness values of all individuals are collected as $F_{\text{all}} = \{F_1, F_2, \ldots, F_N\}$. The mean fitness and minimum fitness values are calculated as

$$\bar{F} = \frac{1}{N}\sum_{i=1}^{N} F_i, \quad F_{\min} = \min\left(F_{\text{all}}\right) \tag{55}$$

where F_i denotes the comprehensive fitness of the i-th individual, and $\bar{F}$ and $F_{\min}$ denote the population mean and minimum comprehensive fitness values, respectively.

Step 2: Calculate the parameter-sensitivity matrix.

A local perturbation analysis is employed to quantify the average influence of a variation in each parameter p_j on the objective fitness:

$$s_{ij} = \Delta Fit_{ij} / \Delta p_{ij}, \quad i = 1, \ldots, N \tag{56}$$

where s_{ij} denotes the sensitivity calculated under a local perturbation; Δp_{ij} denotes the small perturbation applied to an LADRC parameter in the neighborhood of individual i

; and $\Delta \mathrm{Fit}_{ij}$ denotes the corresponding aggregate variation in the multi-objective fitness of the UAV.

After averaging over all individuals, the global parameter-sensitivity vector is obtained as

$$s = [s_1, s_2, \ldots, s_6], \quad s_j = \frac{1}{N}\sum_{i=1}^{N} s_{ij} \tag{57}$$

where s_j denotes the average sensitivity of the j-th controller parameter with respect to the overall flight stability. The parameter-sensitivity perturbation tests are conducted using the complete nonlinear near-flight-envelope dynamic model established in Section 2.2. By slightly perturbing the LADRC controller parameters and observing the resulting changes in closed-loop flight performance, the influence of each parameter on the closed-loop stability of the UAV is quantified.

Step 3: Calculate the individual- and parameter-specific adaptive probabilities.

The crossover and mutation probabilities are independently calculated for each parameter of each individual. For a better-performing individual satisfying $F_i \le \bar{F}$, the base probabilities are calculated as

$$\begin{cases} P_{\mathrm{c,base}}(i) = P_{c,\max} - \left(P_{c,\max} - P_{c,\min}\right) \cdot (\bar{F} - F_i)/(\bar{F} - F_{\min}) \\ P_{\mathrm{m,base}}(i) = P_{m,\max} - \left(P_{m,\max} - P_{m,\min}\right) \cdot (\bar{F} - F_i)/(\bar{F} - F_{\min}) \end{cases} \tag{58}$$

For a poorer-performing individual satisfying $F_i > \bar{F}$, the base probabilities are assigned their maximum values:

$$P_{c,base}(i) = P_{c,max}, \quad P_{m,base}(i) = P_{m,max} \tag{59}$$

where $P_{\mathrm{c,base}}$ and $P_{\mathrm{m,base}}$ denote the base crossover and mutation probabilities, respectively; $P_{\mathrm{c,max}} = 0.5$ and $P_{\mathrm{c,min}} = 0.1$ denote the upper and lower bounds of the crossover probability, respectively; $P_{\mathrm{m,max}} = 0.3$ and $P_{\mathrm{m,min}} = 0.1$ denote the upper and lower bounds of the mutation probability, respectively; and $F_{\min}$ denotes the minimum comprehensive fitness value in the current population.

A sensitivity influence coefficient of $\alpha = 0.5$ is introduced to further reduce the crossover and mutation probabilities of highly sensitive parameters that are more likely to induce oscillations in the UAV closed-loop control system:

$$P_c(i,j) = P_{\mathrm{c,base}}(i) \cdot \left[1 - \alpha \cdot s_j\right], \; P_m(i,j) = P_{\mathrm{m,base}}(i) \cdot \left[1 - \alpha \cdot s_j\right] \tag{60}$$

where $P_{\mathrm{c}}(i,j)$ and $P_{\mathrm{m}}(i,j)$ denote the final adaptive crossover and mutation probabilities applied to the j-th controller parameter of the i-th individual, respectively.

(3) Adaptive Objective-Weight Adjustment

This mechanism dynamically adjusts the evaluation weights in multi-objective optimization according to the convergence of flight-performance objectives such as altitude maintenance and roll tracking. The weights of rapidly converging objectives are reduced, whereas those of slowly converging or deteriorating objectives are increased. This strategy weakens the subjective preference introduced by fixed weights and supports coordinated optimization of multiple objectives, thereby mitigating the weight-allocation imbalance caused by the conflict between rapid attitude response and flight-path altitude maintenance under boundary conditions. For the population at generation t, the adaptive weight-adjustment procedure is defined by Equations (61)–(65) and summarized in Algorithm 1.

Step 1: Calculate the convergence reference value of each objective in the current generation.

The 10 individuals with the best comprehensive performance in each generation are selected as elite individuals, and their mean fitness for each objective is calculated to reduce variation from stochastic simulation evaluations:

$$\bar{f}_k(t) = \frac{1}{10}\sum_{i=1}^{10} f_{k,i}(t), \quad k = 1, \dots, 4 \tag{61}$$

where $\bar{f}_k(t)$ denotes the convergence reference value of the k-th flight-performance objective at generation t, and $f_{k,i}(t)$ denotes the fitness value of the i-th elite individual for the k-th objective at generation t.

Step 2: Calculate the convergence degree of each objective.

To avoid intergenerational fitness oscillations caused by the nonlinear response of the UAV, the convergence reference values separated by four generations are compared. The convergence variation coefficient $CV_k(t)$ of each objective is calculated as

$$CV_k(t) = \frac{\bar{f}_k(t-4) - \bar{f}_k(t)}{\bar{f}_k(t-4)} \tag{62}$$

where $CV_k(t)$ denotes the variation coefficient of the k-th flight-performance objective and represents its relative intergenerational convergence rate. A larger value of $CV_k(t)$ indicates faster convergence.

Step 3: Dynamically adjust the weights according to the convergence degree.

The convergence threshold is set to $\tau = 10^{-3}$, and the weight-adjustment factor $\eta_k(t)$ is calculated as follows. The adjustment factor is constrained to the interval [0.5, 2.0] to prevent abrupt variations in the control-performance evaluation weights from causing abrupt changes in fitness evaluation:

$$\eta_k(t) = \begin{cases} 1 - 5 \times (CV_k(t) - \tau)/\tau, & CV_k(t) > \tau \\ 1 + 3 \times (\tau - CV_k(t))/\tau, & 0 \le CV_k(t) \le \tau \\ 1 + 5 \times |CV_k(t)|/\tau, & CV_k(t) < 0 \end{cases} \tag{63}$$

where $\eta_k(t)$ denotes the weight-adjustment coefficient of the k-th objective. After calculation, $\eta_k(t)$ is clipped to the prescribed interval [0.5, 2.0].

Step 4: Update and normalize the objective weights.

The preliminary weights of the next generation are calculated using the current weights and the adjustment factors: $w_k(t+1) = w_k(t)\eta_k(t)$. The resulting weight vector is then normalized so that the sum of its components remains equal to the sum of the initial base weights:

$$\begin{cases} \tilde{w}_k(t+1) = w_k(t) \cdot \eta_k(t) \\ w_k(t+1) = \dfrac{\tilde{w}_k(t+1)}{\sum_{k=1}^{4} w_k(t+1)} \times \sum_{k=1}^{4} w_k^{\text{base}} \end{cases} \tag{64}$$

where $w_k(t+1)$ denotes the normalized objective-weight vector for the next generation; $\tilde{w}_k(t+1)$ denotes the preliminary adjusted weight of the k-th objective; and w_k^{base} denotes the corresponding component of the initial base-weight vector defined previously.

The updated weight vector is used to calculate the comprehensive fitness of the elite individuals and guide the evolutionary direction of the UAV controller parameters in the next generation:

$$Cphfit_i = \sum_{k=1}^{4} stdrank_i(k) \times w_k(t) \tag{65}$$

where $Cphfit_i$ denotes the comprehensive performance fitness of individual i in the current optimization stage; $\text{stdrank}_i(k)$ denotes the normalized ranking of individual i with respect to the k-th flight-performance objective; and $w_k(t)$ denotes the dynamically updated weight of the k-th objective. Through dynamic weight adjustment, the comprehensive fitness more accurately reflects the relative control performance of an individual under the current flight condition.

For clarity, the four-step adaptive objective-weight adjustment procedure defined by Equations (61)–(65) is summarized in Algorithm 1. Given the current population, the current objective-weight vector, and the initial base-weight vector, Algorithm 1 selects the elite individuals, updates and normalizes the objective weights, and evaluates the comprehensive fitness.

Algorithm 1: The Adaptive Weight-Adjustment Procedure

Require: Current population at generation t, current objective-weight vector $W(t)$, initial base-weight vector W_{base}, and convergence threshold $\tau = 10^{-3}$.

Ensure: Normalized objective-weight vector $W(t+1)$ and comprehensive fitness. $Cphfit_i$

Select the 10 individuals with the best comprehensive performance and compute their objective-wise mean fitness for $k = 1, \ldots, 4$ using Equation (61).
Compute the convergence variation coefficient $CV_k(t)$ over the four-generation interval using Equation (62).
Calculate the weight-adjustment factor $\eta_k(t)$ using Equation (63), and clip it to $[0.5,\ 2.0]$.
Update and normalize $W(t+1)$ using Equation (64), and evaluate $Cphfit_i$ using Equation (65).
return $W(t+1)$, $Cphfit_i$

The complete hierarchical adaptive NSGA-II procedure is summarized in Algorithm 2. During Stage II, Algorithm 2 invokes Algorithm 1 to update the objective weights and comprehensive fitness. Algorithm 2 links the two stages to the LADRC controller and nonlinear flight-dynamics simulation. The pseudocode lists the required inputs, stage-specific updates, convergence checks, and final output following the workflow shown in Figure 6.

Algorithm 2: Hierarchical Adaptive NSGA-II for LADRC Parameter Tuning

Require: Constraint boundaries of the LADRC controller parameters, population size N, number of pre-optimization generations G_1, number of multi-objective coordinated optimization generations G_2, and initial objective-weight vector W_0.

Ensure: Pareto-optimal solution set of the LADRC controller parameters.

// Stage 1: Hierarchical Single-Objective Pre-Optimization

Initialize four independent single-objective populations Pop_i, $i = 1,2,3,4$, corresponding to the four optimization objectives of altitude deviation, airspeed tracking, roll-tracking accuracy, and roll oscillation, respectively.
for $g = 1$ to do
    for $i = 1$ to 4 do
        Conduct a closed-loop simulation based on the six-degrees-of-freedom nonlinear flight-dynamics model and the LADRC controller.

Evaluate the single-objective fitness of each individual in Pop_i according to Equation (49).

Perform selection, crossover, and mutation operations to generate the updated offspring population Pop_i.

end for

end for

Select the 10 individuals with the best fitness values from each population Pop_i and merge them to form the initial population for the multi-objective stage: $\mathrm{Pop} = \bigcup_{i=1}^{4} \mathrm{Pop}_i^{\mathrm{top10}}$.

// Stage 2: Multi-Objective Coordinated Optimization

for $g = 1$ to G_2 do

// Mechanism 1: Adaptive Parameter-Range Adjustment

Select the top 20% elite individuals from Pop and construct the elite parameter-feature matrix E.

Dynamically reshape the encoding boundaries of each parameter using Equations (50)–(54), according to the distribution characteristics of E and the current iteration progress g / G_2.

// Mechanism 2: Adaptive Crossover and Mutation Probabilities

Calculate the mean fitness F_{avg} and minimum fitness $F_{\min}$ of the current population Pop.

Evaluate the global sensitivity vector S of the six LADRC parameters for all three channels using the local perturbation method.

Independently generate the adaptive crossover probability P_c and mutation probability P_m using Equations (55)–(60), based on the individual fitness and the parameter-sensitivity vector S.

// Mechanism 3: Adaptive Objective-Weight Adjustment

Invoke Algorithm 1 with the current population, $W(t)$, W_{base}, and τ to obtain $W(t+1)$ and Cphfit_i using Equations (61)–(65).

// Standard NSGA-II Evolution and Environmental Selection

Perform binary tournament selection, crossover, and mutation according to P_c and P_m to generate the offspring population Off.

Merge the parent and offspring populations: $\mathrm{Pop}_{\mathrm{total}} = \mathrm{Pop} \cup \mathrm{Off}$.

Perform fast non-dominated sorting on $\mathrm{Pop}_{\mathrm{total}}$ and calculate the crowding distance of each individual.

Select and retain N individuals according to their non-dominated ranks and crowding distances to generate the next-generation population Pop.

end for

return the first non-dominated front in Pop, i.e., the solution set satisfying $\mathrm{Rank} = 1$.

4. Simulation Experiments and Flight-Test Result Analysis

4.1. Simulation Experiment Setup

This section outlines the simulation environment, operating-condition constraints, and experimental evaluation scheme to verify the performance of the improved multi-objective genetic algorithm and the LADRC controller.

4.1.1. Simulation Environment and Modeling Basis

Simulations are conducted in MATLAB/Simulink R2022b using a fixed-step fourth-order Runge–Kutta (RK4) numerical solver with a step size of 0.005 s. The dynamic model adopts the previously derived six-degrees-of-freedom rigid-body UAV model, incorporating complete aerodynamic expansions to reproduce lateral–longitudinal coupling and nonlinear degradation of aerodynamic damping during large-angle maneuvers near the flight-envelope boundary. The fundamental modeling assumptions are as follows:

(1) The UAV is treated as a rigid body, neglecting structural elastic and aeroelastic coupling effects;
(2) High-frequency sensor noise is excluded to primarily evaluate the controller's disturbance rejection and parameter perturbation suppression capabilities;
(3) Engine thrust dynamics are simplified as a first-order inertial element.

4.1.2. Operating-Condition Parameters and Constraint Configuration

The baseline operating condition is set near the flight-envelope boundary at an altitude of 5500 m and an airspeed of 150 m/s, corresponding to a high-altitude, low-density regime in which dynamic pressure varies with altitude and external disturbances. External disturbances combine moderate atmospheric turbulence specified by military standards with 15 m/s discrete gusts to represent the strong wind shear in mountainous valleys. As defined in Section 3.4.1, the three channels contain nine scheduled LADRC gains represented by 18 slope and intercept coefficients, while each sequential channel optimization uses six coefficients; Table 2 gives their bounds.

The simulation incorporates actuator physical constraints, with maximum elevator, aileron, and rudder deflections of ±20° and a natural bandwidth of 40 rad/s. The test task involves three consecutive alternating roll reversals, with the command amplitude dynamically calculated based on the maximum allowable normal load to effectively excite large-angle aerodynamic coupling effects.

4.1.3. Experimental Scheme and Evaluation Indices

The experiments are conducted in three sequential stages:

(1) Nominal simulation without parameter perturbations: This verifies the fundamental performance of the control architecture and serves as a baseline for subsequent perturbation comparisons.
(2) Multi-objective optimization experiments: The improved multi-objective genetic algorithm is run independently 30 times to compare optimization results and verify the algorithm's convergence stability.
(3) Robustness simulations under multi-source parameter perturbations: Latin hypercube sampling generates 100 sample sets. Using the optimal control parameters, four categories of perturbations—aerodynamic, inertial, actuator, and combined full-parameter—are applied to quantitatively evaluate stability boundaries and performance degradation.

Flight performance is quantitatively evaluated using four principal indices $J_1 \sim J_4$, with complete definitions and calculation formulas detailed in Section 3.3. Since the lateral-directional aerodynamic coupling and nonlinear damping degradation induced by continuous large-angle maneuvers near the envelope boundary represent the primary

https://doi.org/10.3390/drones10070532

constraints on flight safety, subsequent analyses—including convergence profiling, robustness statistics, and field flight-test verification—primarily focus on the dynamic response and tracking accuracy of the main roll channel. The coordinated stabilization effects of the pitch and yaw channels are additionally supported by comprehensive indices such as altitude deviation and airspeed tracking.

4.2. Verification of Optimization Performance and Stability

Thirty independent optimization runs were conducted using the improved multi-objective genetic algorithm. As shown in Figure 7, the red solid trajectory after optimization is smoother than the blue dashed trajectory before optimization, and its turning radius R is larger. For a coordinated level turn, the trajectory radius of curvature R and the normal load factor n satisfy the relationship $n = 1 + V^2/(gR)$ (where V is the airspeed). At constant airspeed, increasing the radius limits the normal load factor, which can reduce high-frequency attitude oscillations, control-surface overshoot, alternating fatigue loads, and the likelihood of entering the stall regime. The red trajectory therefore suggests a larger stability margin. The overlapping trajectories from the 30 runs are also relatively compact, indicating consistent convergence across runs.

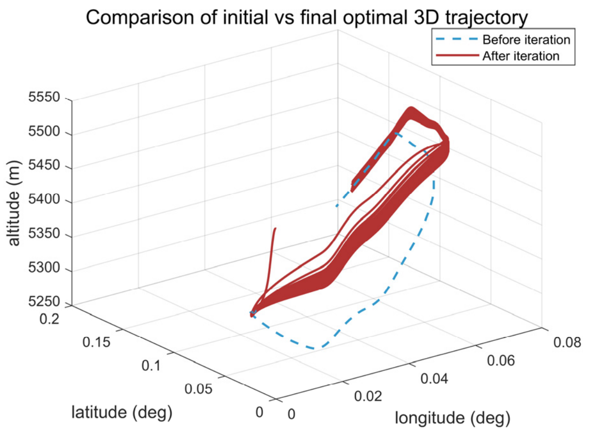

Figure 7. Comparison of three-dimensional flight trajectories before and after optimization.

Combining the trajectory characteristics in Figure 7 with the local time-domain roll-angle curves in Figure 8, the control dynamics are improved across three stages:

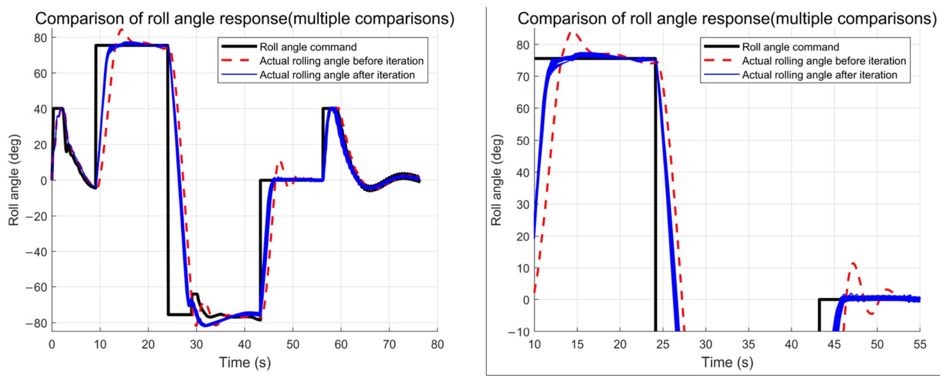

Figure 8. Comparison of roll-angle time-domain responses before and after optimization.

(1) Transient tracking stage (as shown in the left panel of Figure 8): After optimization, the nonlinear lag and large oscillations caused by gain mismatch are reduced, improving transient tracking and corresponding to the absence of apparent spatial distortion in the red solid trajectory at the beginning of Figure 7.

(2) Overshoot convergence stage (as shown in the left panel of Figure 8): The unoptimized controller may cause actuator saturation and aerodynamic instability, whereas the overshoot after optimization is limited, improving the system damping characteristics.
(3) Steady-state maintenance stage (as shown in the right panel of Figure 8): The optimization suppresses low-frequency residual oscillations induced by lateral–longitudinal coupling, and the steady-state tracking error is reduced.

The seven auxiliary roll-response indices defined in Section 3.3.2 are used to quantify the before/after comparison. The baseline uses manual empirical tuning, whereas the post-optimization results use the mean optimal parameters from 30 independent runs. Table 3 and Figure 9 report the comparison.

Table 3. Comparison of roll-angle control performance before and after 30 optimization runs.

Performance Index	Before Optimization (Experience-Based Tuning)	After Optimization (Mean ± Standard Deviation)	Improvement
Rise time (s)	2.4375	1.8993 ± 0.0770	Reduced by 22.1%
Percentage overshoot (%)	10.57	0.30 ± 0.36	Reduced by 97.1%
Settling time (s)	4.9975	2.6531 ± 0.1511	Reduced by 46.9%
Steady-state error (rad)	0.074330	0.004676 ± 0.003418	Reduced by 93.7%
RMS tracking error (rad)	0.544676	0.430792 ± 0.014287	Reduced by 20.9%
Integral absolute error (rad·s)	17.3496	11.7704 ± 0.5452	Reduced by 32.2%
Control energy (rad^2/s)	4.4197	4.6569 ± 0.6695	Increased by 5.4%

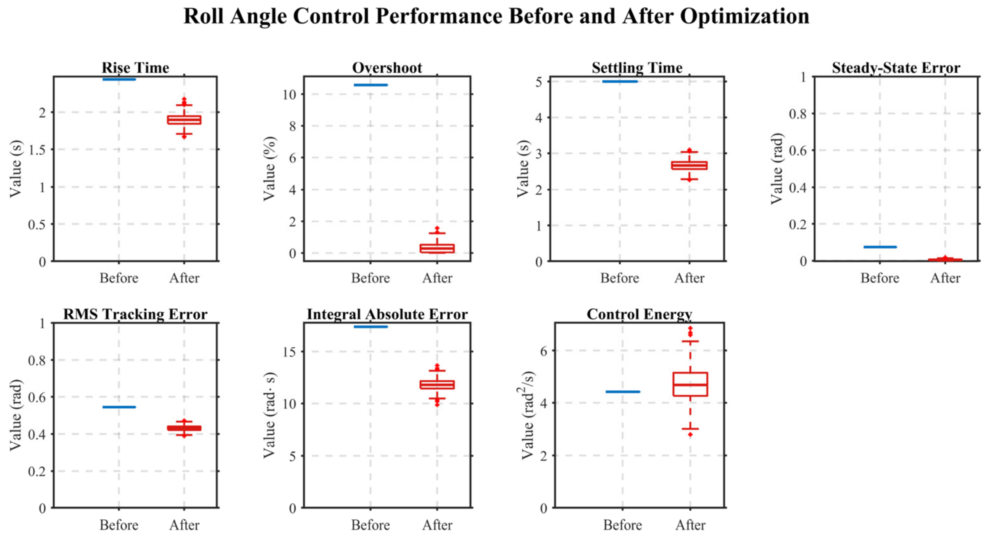

Figure 9. Boxplots of the control-performance indices from 30 independent optimization runs.

Combining the quantitative data in Table 3 and the distribution characteristics in Figure 9, the comparison results indicate:

(1) Improved transient response quality: As shown in Table 3, the percentage overshoot decreases from 10.57% to 0.30% (a reduction of 97.1%), and roll oscillations are reduced. The settling time is shortened by 46.9%, and the steady-state error is reduced by 93.7%, showing improvements in both convergence speed and steady-state accuracy under command changes.
(2) Enhanced full-duration tracking performance: As shown in Table 3, the full-duration RMS tracking error decreases by 20.9%, and the integral absolute error decreases by 32.2%, improving the overall trajectory tracking accuracy.

(3) Stable optimization performance: As shown in Figure 9, the interquartile ranges of the boxplots are narrow with only limited outliers. Combined with the relatively small standard deviations in Table 3, this indicates that the algorithm is relatively insensitive to random initialization and produced consistent parameter solutions across the tested runs.

4.3. Verification of Controller Robustness Under Multi-Source Perturbations

To verify the robustness of the optimized control parameters under model uncertainties, the four indices defined in Section 3.3 (maximum altitude deviation J_1, airspeed-tracking RMSE J_2, roll-tracking RMSE J_3, and roll-oscillation index J_4) are adopted for quantitative evaluation. Using the nominal perturbation-free condition as a baseline, Latin hypercube sampling is used to generate 100 sample sets for four perturbation scenarios: aerodynamic, inertial, actuator, and combined full-parameter perturbations. The parameter perturbation types and ranges are detailed in Table 4 (where C_{lr} and C_{np} are assigned random-sign perturbations to simulate instability scenarios at high angles of attack near the envelope).

Table 4. Types and ranges of uncertain parameter perturbations.

Parameter Category	Parameter Symbol	Physical Meaning	Perturbation Form	Perturbation Range
Aerodynamic parameters	$\bar{q}$	Flight dynamic pressure	Relative gain	±10%
	$C_m^{\delta_e}$	Elevator pitch control moment derivative	Relative gain	±20%
	C_{mq}	Pitch rate damping moment derivative	Relative gain	±80%
	$C_{m\alpha}$	Angle of attack static stability moment derivative	Relative offset	±20%
	$C_L^{\delta_e}$	Elevator lift control derivative	Relative gain	±20%
	C_{Lq}	Pitch rate lift derivative	Relative gain	±20%
	$C_{L\alpha}$	Angle of attack lift curve slope	Relative offset	±10%
	$C_{Y\beta}$	Sideslip angle side force derivative	Relative offset	±20%
	$C_Y^{\delta_r}$	Rudder side force control derivative	Relative gain	±20%
	C_{Yp}	Roll rate side force derivative	Relative gain	±50%
	C_{Yr}	Yaw rate side force derivative	Relative gain	±50%
	$C_{l\beta}$	Sideslip angle roll static derivative	Relative offset	±20%
	$C_l^{\delta_a}$	Aileron roll control moment derivative	Relative gain	±20%
	C_{lr}	Yaw rate roll cross derivative	Random sign, relative gain	Random sign, amplitude ±80%
	$C_l^{\delta_r}$	Rudder roll control moment derivative	Relative gain	±20%
	C_{lp}	Roll rate damping moment derivative	Relative gain	±80%
	$C_{n\beta}$	Sideslip angle yaw static derivative	Relative offset	±20%
	$C_n^{\delta_r}$	Rudder yaw control moment derivative	Relative gain	±20%
	$C_n^{\delta_a}$	Aileron yaw control moment derivative	Relative gain	±20%
	C_{np}	Roll rate yaw cross derivative	Random sign, relative gain	Random sign, amplitude ±80%
	C_{nr}	Yaw rate damping moment derivative	Relative gain	±80%
Inertial parameters	I_x, I_y, I_z	Three-axis moments of inertia	Absolute offset	I_x: ±3 kg·m² I_y, I_z: ±30 kg·m²
	I_{xz}	Roll–yaw product of inertia	Absolute offset	±1.8 kg·m²
	x_{cg}	CG axial offset	Absolute offset	±6.6 mm

https://doi.org/10.3390/drones10070532

Servo parameters	ω_n	Servo natural bandwidth	Absolute offset	40~80 rad/s
	τ_d	Servo response delay	Absolute offset	0.02~0.06 s

Pitch-angle and normal-load closed-loop control are selected as the evaluation tasks. The following analysis primarily focuses on the pitch closed-loop (as the normal load closed-loop follows consistent patterns). The statistical data of the indices are presented in Table 5, and the corresponding distribution boxplots are shown in Figure 10.

Table 5. Statistical results of control-performance indices under multi-source perturbations.

Performance Index	Perturbation Scenario	Nominal Value	Mean	95th Percentile	Maximum Value	Standard Deviation	Coefficient of Variation
J_1: Maximum altitude deviation (m)	Nominal baseline	26.877	-	-	-	-	-
	Aerodynamic	-	27.281	30.145	35.181	1.519	0.056
	Inertial	-	26.735	27.007	27.061	0.182	0.007
	Actuator	-	**26.719**	26.755	26.877	0.029	0.001
	Combined	-	27.304	29.912	35.847	1.566	0.057
J_2: Airspeed-tracking RMSE (m/s)	Nominal baseline	6.44	-	-	-	-	-
	Aerodynamic	-	9.526	14.013	23.259	2.868	0.301
	Inertial	-	6.402	6.531	6.543	0.083	0.013
	Actuator	-	**6.397**	6.406	6.44	0.007	0.001
	Combined	-	9.527	13.936	24.566	2.907	0.305
J_3: Roll-tracking RMSE (°)	Nominal baseline	0.806	-	-	-	-	-
	Aerodynamic	-	**0.763**	1.081	1.861	0.206	0.27
	Inertial	-	0.774	0.899	0.937	0.064	0.083
	Actuator	-	0.812	1.202	1.202	0.151	0.186
	Combined	-	0.87	1.802	3.199	0.419	0.482
J_4: Roll-oscillation index (°)	Nominal baseline	0.804	-	-	-	-	-
	Aerodynamic	-	**0.766**	1.073	1.713	0.182	0.237
	Inertial	-	0.772	0.879	0.902	0.055	0.071
	Actuator	-	0.805	1.147	1.147	0.13	0.161
	Combined	-	0.856	1.688	2.793	0.355	0.414

Note: Lower values indicate better performance for all four indices. Bold values are the lowest mean among the four perturbation scenarios for each index.

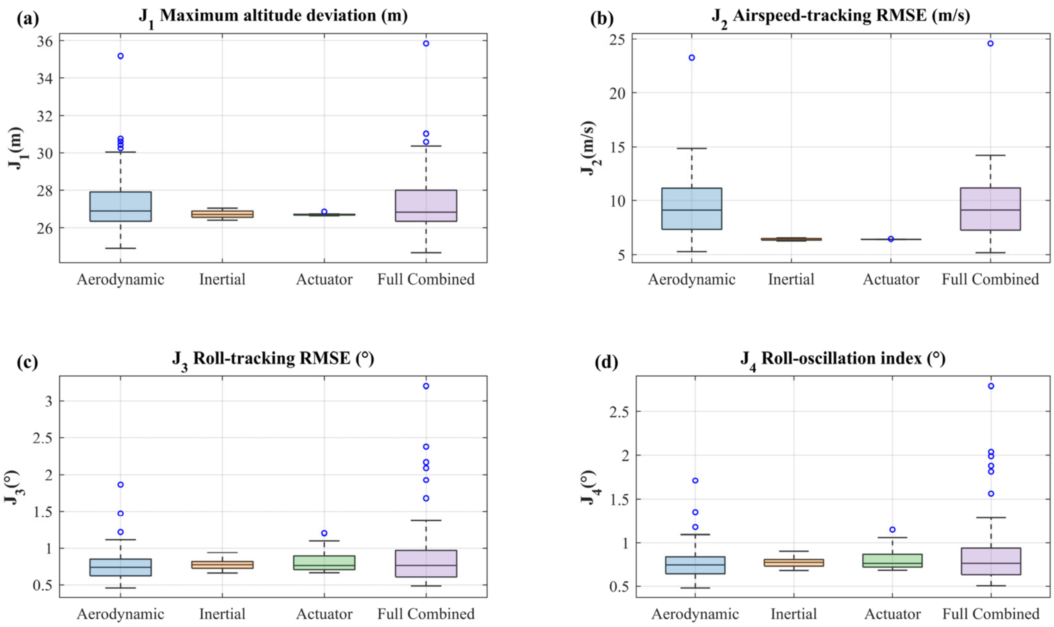

Figure 10. Distributions of J_1–J_4 under multi-source parameter perturbations: (**a**) maximum altitude deviation; (**b**) airspeed-tracking RMSE; (**c**) roll-tracking RMSE; (**d**) roll-oscillation index.

Combining Table 5 and Figure 10, aerodynamic parameter perturbations have a greater impact on control performance: the airspeed tracking RMSE increases by approximately 47.9%, while the altitude and roll indices experience minor degradation, which is consistent with the physical characteristics of aerodynamic damping degradation and nonlinear variations in control effectiveness near the envelope. Under inertial and actuator perturbations, the mean deviations of all indices are below 5% with relatively small coefficients of variation, indicating that the total disturbance estimation and feedforward compensation mechanism of LADRC mitigates such disturbances. Under the combined full-parameter perturbation condition, the 95th percentiles of the tracking indices remain within engineering-acceptable ranges, and no samples exhibit closed-loop instability. As illustrated in Figure 10, the aerodynamic and combined perturbation groups show larger dispersion (with outliers corresponding to large deviations in aerodynamic derivatives), whereas the inertial and actuator groups exhibit narrower boxes, consistent with the statistical patterns in Table 5.

The multi-channel time-domain response envelopes under the combined full-parameter perturbation are shown in Figures 11 and 12:

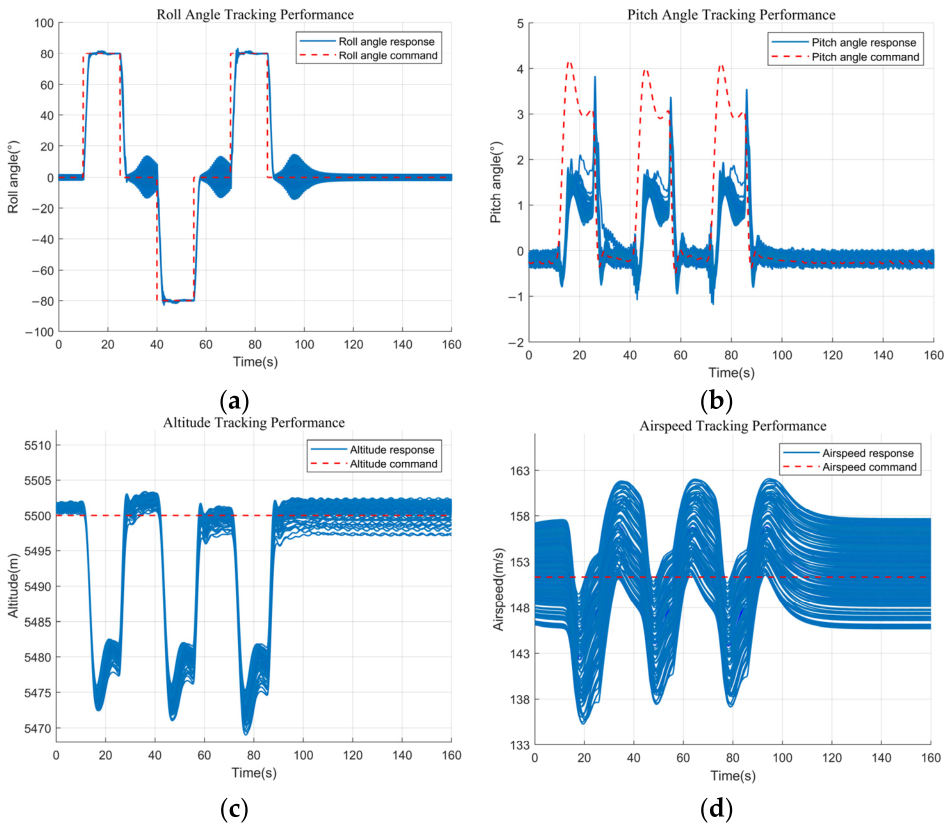

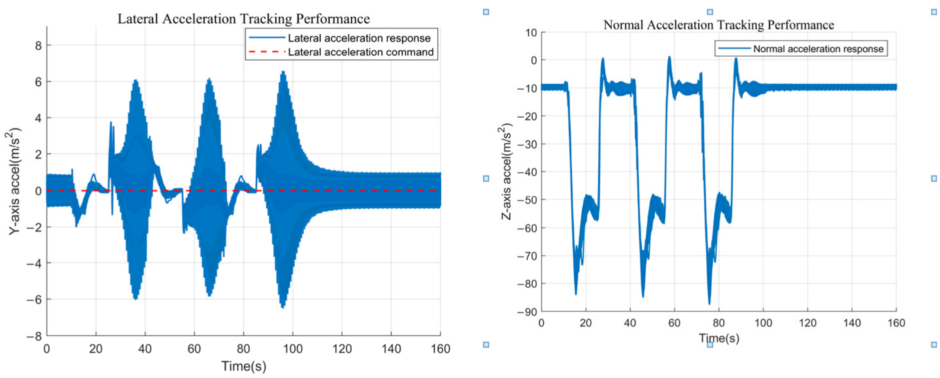

(e) (f)

Figure 11. Multichannel tracking responses under combined full-parameter perturbations with pitch-angle closed-loop control: (**a**) roll angle; (**b**) pitch angle; (**c**) altitude; (**d**) airspeed; (**e**) lateral acceleration; (**f**) normal acceleration.

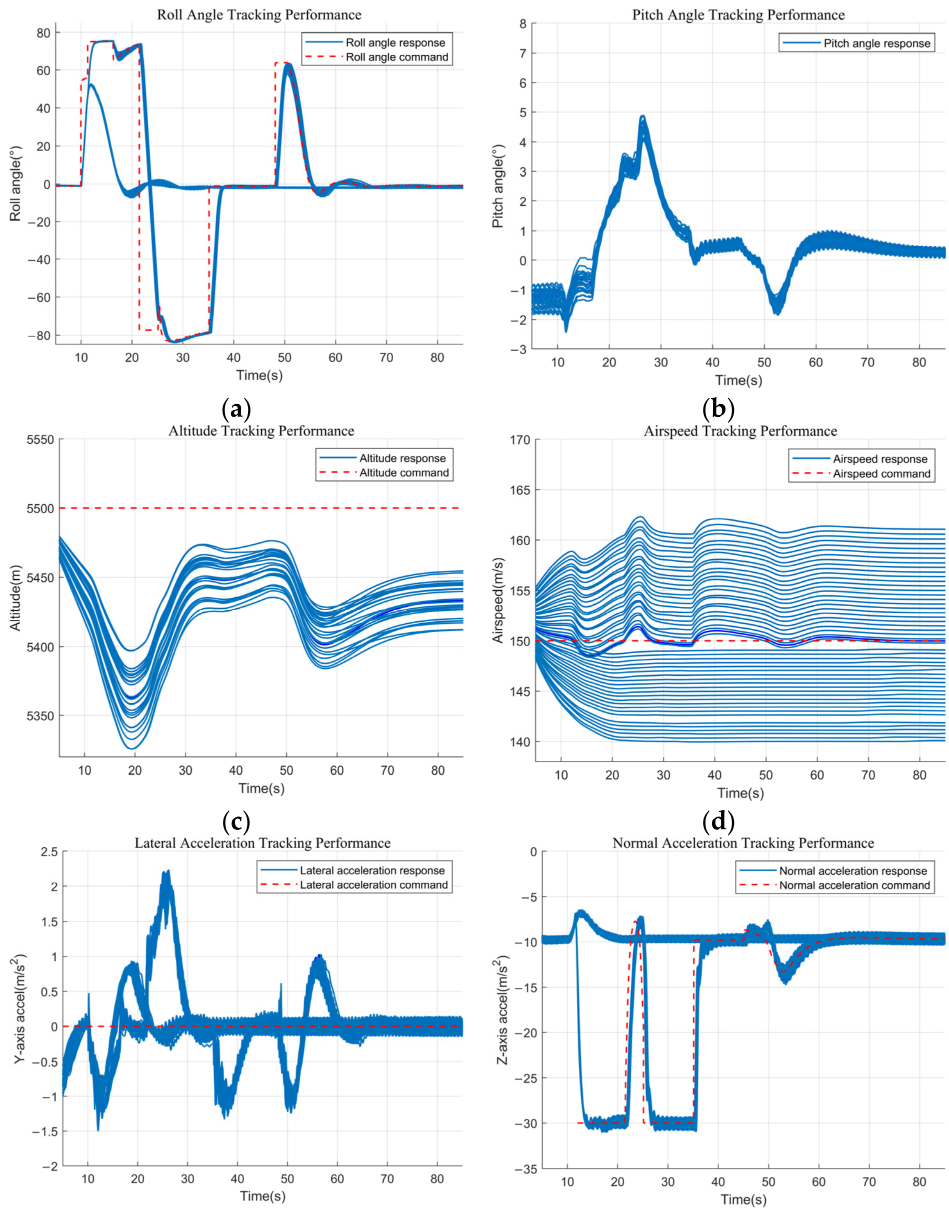

Figure 12. Multichannel tracking responses under combined full-parameter perturbations with normal-load closed-loop control: (**a**) roll angle; (**b**) pitch angle; (**c**) altitude; (**d**) airspeed; (**e**) lateral acceleration; (**f**) normal acceleration.

(1) Based on the pitch closed-loop responses in Figure 11, the roll reversals are smooth, and the responses are consistent with real-time compensation of parameter deviations and coupling disturbances by the LESO. The pitch channel exhibits only small, rapidly converging transient fluctuations during maneuver switching. Although the altitude and airspeed sample bands widen under dynamic-pressure disturbances, the trajectories remain regulated around the baseline, and the lateral- and normal-load responses show no visible limit exceedances.
(2) Based on the normal-load closed-loop responses in Figure 12, the built-in maneuver-entry and envelope-exit protection logic reduces stall risk. Most samples smoothly track the normal-load commands, while some samples with large aerodynamic deviations maintain stable level flight after triggering the protection. Owing to strong aerodynamic coupling, the altitude and airspeed response envelopes are wider than those under pitch-angle closed-loop control.

In summary, Table 5 and Figures 10–12 show that the optimized LADRC controller remained closed-loop stable under the tested multi-parameter perturbations. Performance degradation stayed within an acceptable range, supporting robustness under the tested near-envelope scenarios.

4.4. Verification of the Effectiveness of the Algorithmic Improvements

This section evaluates the optimization performance of the improved NSGA-II incorporating hierarchical pre-optimization and a threefold adaptive mechanism from four aspects: mechanism-based comparison with benchmark algorithms, single-component and combined ablation studies, repeated-run statistical analysis, and computational cost. All comparative experiments used the same population size, maximum generations, and total number of flight-dynamics simulation calls to avoid bias from unequal computational budgets. The performance criteria were $J_1 - J_4$, as defined in Section 3.3, consistent with those used for the robustness evaluation in Section 4.3. The repeated-run statistics of the improved algorithm were based on 30 independent runs. The four algorithm-comparison metrics are defined in Section 3.3.3 and numbered as Equations (40)–(43).

4.4.1. Mechanism-Based Comparison with External Benchmark Algorithms and Single-Component Ablation Verification

The standard NSGA-II without hierarchical or adaptive mechanisms was selected as the ablation baseline. Hierarchical pre-optimization, adaptive parameter ranges, adaptive crossover and mutation probabilities, and adaptive objective weights were then introduced individually. The statistical results are presented in Table 6, and the convergence curves of the four objectives are shown in Figure 13.

The results show that all four components reduced the comprehensive fitness, although their primary effects differed. Hierarchical pre-optimization produced the largest overall improvement. Adaptive crossover and mutation probabilities balanced convergence speed and stability. Adaptive parameter ranges mainly reduced iterative fluctuations and parameter dispersion, whereas adaptive objective weights coordinated the trade-offs among altitude, airspeed, roll tracking, and roll oscillation.

Table 6. Statistical results of the comprehensive multi-objective fitness with individual improvement modules.

Added Component	J_{final}	t_{conv}	CV	$\eta(\%)$
Standard NSGA-II	1.603×10^5	21	0.004409574	0
Hierarchical pre-optimization only	1.532×10^5	12	0.002016313	4.414274173
Parameter interval adaptation only	1.601×10^5	46	0.003104792	0.127183926
Crossover/mutation probability adaptation only	1.582×10^5	11	0.000787876	1.118103903
Objective weight adaptation only	1.599×10^5	33	0.003058667	0.220291883

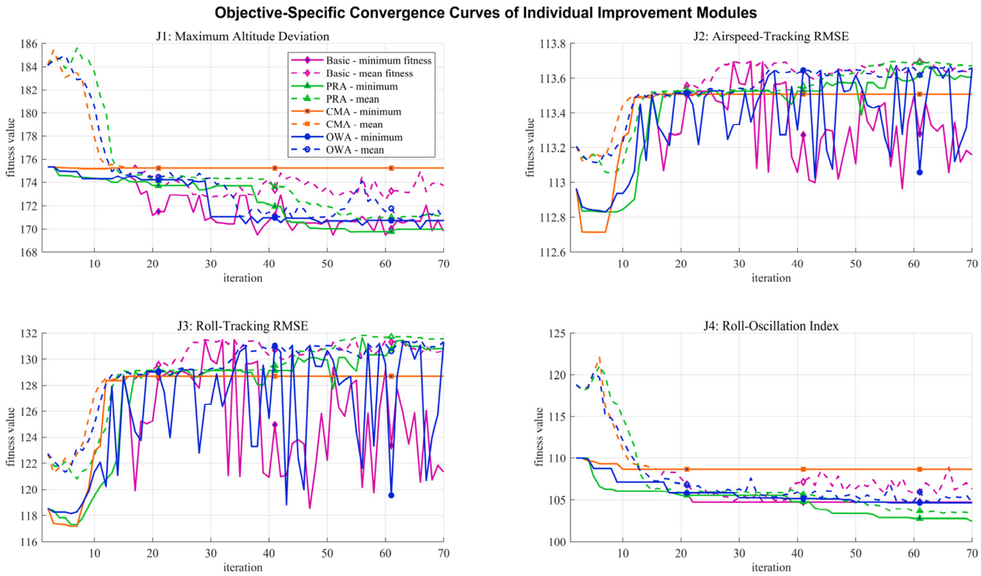

Figure 13. Objective-specific convergence comparison of individual improvement modules. Basic: standard NSGA-II; PRA: parameter-range adaptation; CMA: crossover/mutation-probability adaptation; OWA: objective-weight adaptation. Solid lines denote minimum fitness, and dashed lines denote mean fitness.

More specifically, hierarchical pre-optimization allowed the multi-objective stage to start from lower fitness levels and reduced the number of early search generations. Adaptive crossover and mutation probabilities improved the convergence of all four objectives and particularly improved the roll-oscillation criterion. Adaptive objective weights primarily coordinated long-duration altitude and airspeed tracking, whereas adaptive parameter ranges reduced the dispersion of the controller parameters by progressively adjusting the search intervals.

Among commonly used multi-objective algorithms, the reference-point mechanism of NSGA-III is generally intended for many-objective problems and may provide limited additional benefit for the four-objective problem considered here. Fixed decomposition weights in MOEA/D may restrict balanced exploration of non-convex flight-control optimization problems, whereas MOPSO may be sensitive to premature convergence in continuous high-dimensional parameter spaces. Standard NSGA-II therefore provides a baseline consistent with the framework and optimization mechanisms of the present study. This is a mechanism-based suitability analysis; a complete quantitative comparison across algorithms is reserved for future work.

4.4.2. Combined Ablation Verification of the Hierarchical Framework and Threefold Adaptive Mechanism

To distinguish the individual contributions and combined effects of hierarchical pre-optimization and the threefold adaptive mechanism, hierarchical pre-optimization alone was used as the common baseline, after which the adaptive mechanisms were added progressively. The total number of flight-dynamics simulation calls was kept identical among all configurations to reduce comparison bias caused by unequal computational budgets.

(1) Independent contribution of hierarchical pre-optimization

As shown in Figure 14, the hierarchical framework first divides the four flight-control criteria into separate single-objective subpopulations. Each subpopulation is pre-optimized toward a lower-fitness parameter region before the populations are merged to form the initial multi-objective population. This procedure reduces the evaluation of low-quality parameter combinations during the multi-objective stage.

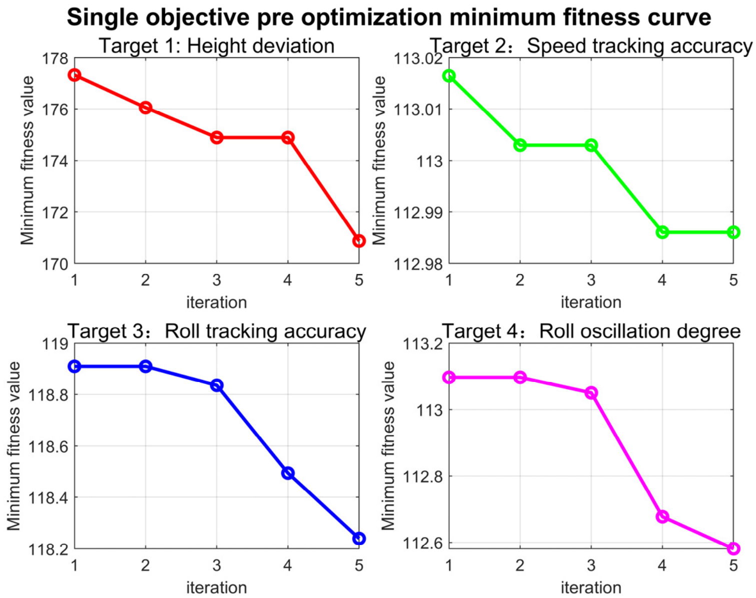

Figure 14. Convergence of single-objective subpopulations during hierarchical pre-optimization.

To compare random initialization with hierarchical pre-optimization, the four criteria of the first-generation individuals were normalized, as shown in Figure 15. Randomly initialized individuals were distributed relatively evenly across the criteria, whereas hierarchically pre-optimized individuals performed better on different objectives, thereby expanding the coverage of the initial parameter space.

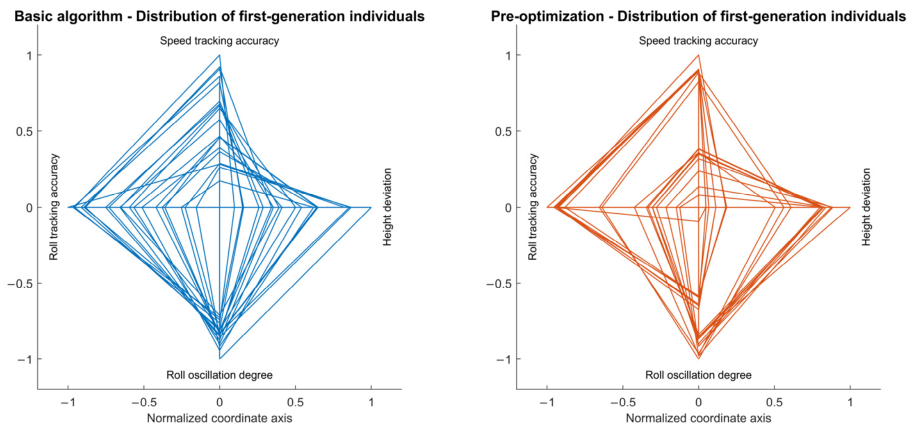

Figure 15. Comparison of initial-population performance distributions between random initialization and hierarchical pre-optimization.

These objective-specialized initial individuals provide a broader set of candidate parameters for subsequent multi-objective recombination and reduce the likelihood of premature population concentration in a limited region. Using the standard NSGA-II crowding-distance calculation, the mean crowding distance increased from 0.3688 under random initialization to 0.3990 after hierarchical pre-optimization, corresponding to a relative increase of 8.19% and indicating greater initial solution-set diversity.

Under the same total simulation budget, the multi-objective convergence processes with and without hierarchical pre-optimization are compared in Figure 16. Because the hierarchical algorithm includes a preliminary single-objective stage, its multi-objective convergence curve begins after pre-optimization. The hierarchical mechanism reduced fitness fluctuations and the gap between the best and mean fitness values while accelerating subsequent multi-objective convergence.

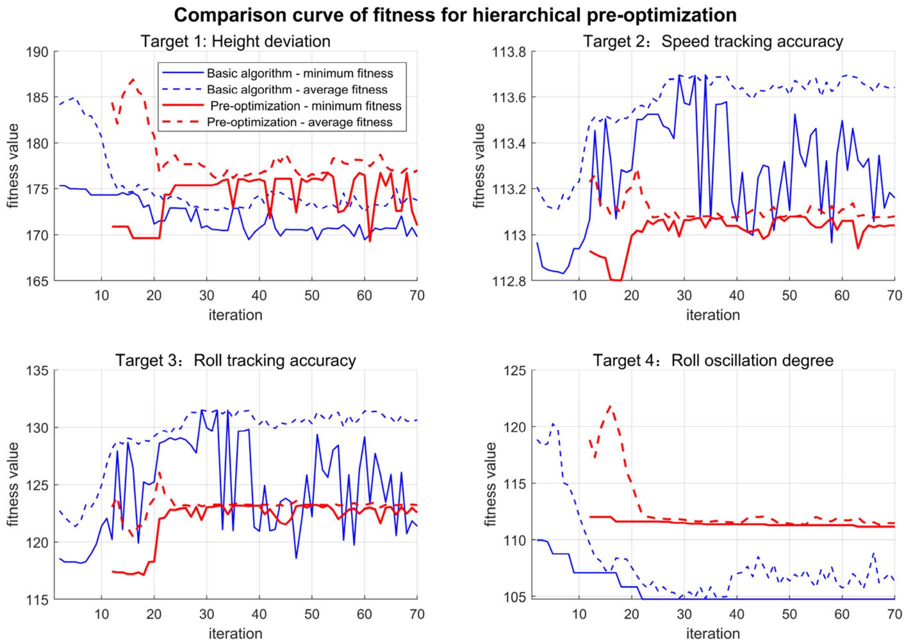

Figure 16. Multi-objective convergence comparison with and without hierarchical pre-optimization.

The comprehensive fitness decreased from 1.603×10^5 for standard NSGA-II to 1.532×10^5, corresponding to an improvement of approximately 4.41%. This result indicates that hierarchical initialization enables the population to enter feasible parameter regions earlier and reduces inefficient exploration during the multi-objective stage.

From a flight-control perspective, earlier convergence of the altitude and airspeed criteria can reduce state deviations caused by changes in thrust, lift, and dynamic pressure. Improvements in roll tracking and roll oscillation can also reduce attitude fluctuations and additional loads during crosswind maneuvers.

(2) Quantitative Combined Ablation Analysis of the Threefold Adaptive Mechanism

The combined ablation results using hierarchical pre-optimization alone as the baseline are presented in Table 7.

Table 7. Ablation results of adaptive components under the hierarchical pre-optimization framework.

Optimization Configuration	Final Convergence Value	Convergence Generation	Coefficient of Variation	Relative Improvement Rate
Hierarchical pre-optimization only	153,223.9185	11	0.0020	0
Hierarchical + parameter-range adaptation	153,200.2580	11	0.0012	0.02
Hierarchical + crossover/ mutation-probability adaptation	153,061.9527	10	0.0009	0.11

Hierarchical + objective-weight adaptation	153,103.9102	32	0.0009	0.08
Hierarchical + all threefold adaptive components	153,096.0876	11	0.0006	0.08

As shown in Table 7, adaptive crossover and mutation probabilities produced the smallest J_{final} and the lowest number of generations to convergence. Adaptive parameter ranges mainly reduced CV from 0.0020 to 0.0012. Adaptive objective weights improved both comprehensive fitness and fluctuation level, although the convergence generation increased to 32.

Relative to hierarchical pre-optimization alone, the complete configuration reduces final fitness from 153,223.9185 to 153,096.0876, a further 0.083%, while the post-convergence coefficient of variation decreases from 0.0020 to 0.0006, a 70% reduction. Thus, the principal contribution of the threefold adaptive mechanism is improved post-convergence stability and consistency rather than an additional large reduction in final fitness.

Adaptive parameter ranges constrain parameter variations, adaptive crossover and mutation probabilities improve search efficiency, and adaptive objective weights coordinate conflicting objectives. The main contribution of the complete configuration is reduced post-convergence fitness fluctuation rather than the minimum final convergence value alone.

Under the same computational budget, the convergence curves obtained by disabling each adaptive mechanism individually are shown in Figure 17. All configurations approached stable values after approximately 15 generations. Adaptive parameter ranges mainly reduced fluctuations after generation 10. Adaptive crossover and mutation probabilities improved final fitness and population stability at a similar convergence rate. Adaptive objective weights enabled limited escape from local optima during the converged stage.

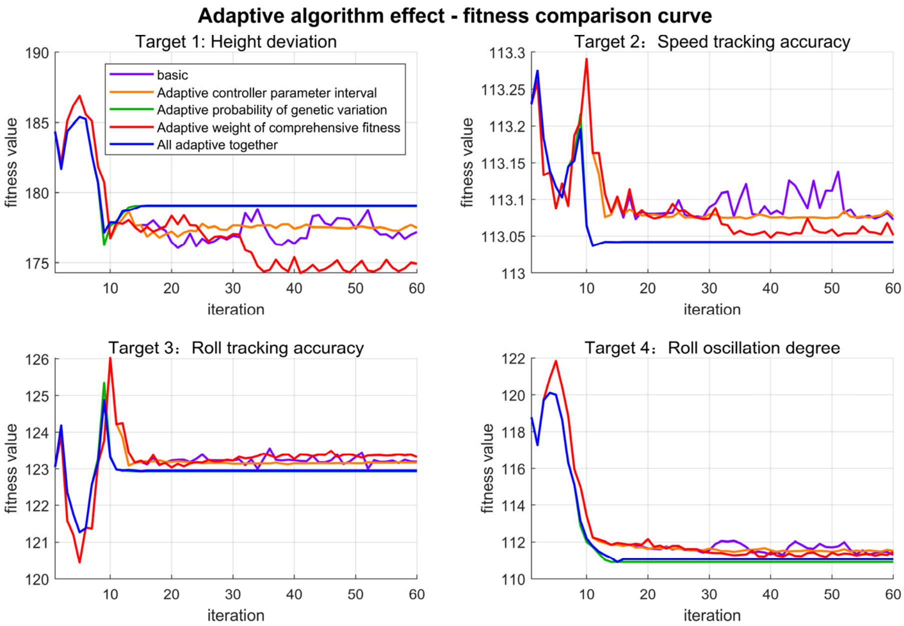

Figure 17. Multi-objective convergence characteristics across adaptive component combinations.

Compared with hierarchical pre-optimization alone, the complete algorithm produced lower comprehensive fitness and reduced fluctuation. Its convergence-curve shape was primarily governed by the adaptive crossover and mutation mechanism, while the other two mechanisms provided search-range regulation and objective coordination.

As shown in Figure 17, three objectives continued to decrease during the later iterations, whereas the roll-tracking criterion fluctuated around an approximately constant level. This behavior reflects a multi-objective trade-off between suppressing lateral–longitudinal coupling during large maneuvers and maintaining roll-angle tracking accuracy.

The parallel-coordinate distributions of the Pareto-front individuals at different generations are shown in Figure 18. As the iterations proceeded, the differences among the objectives decreased, and the solution set moved toward a region with lower comprehensive fitness and a more balanced objective distribution.

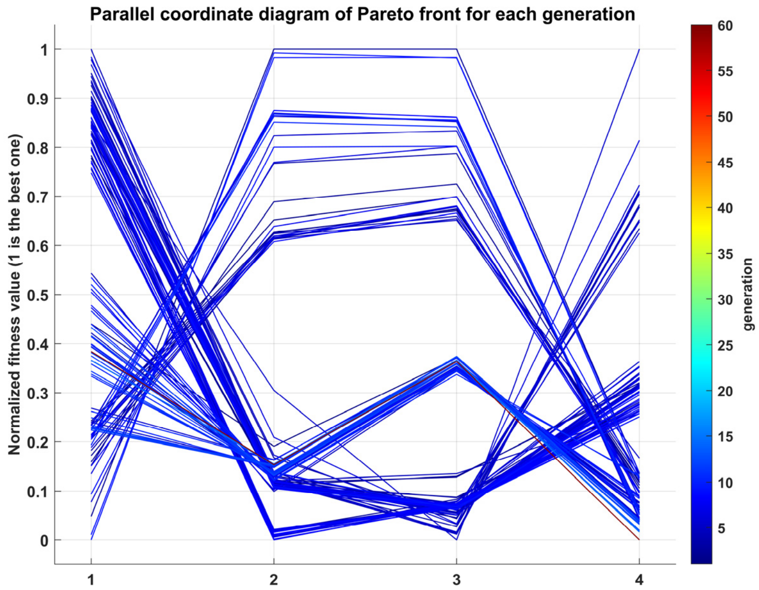

Figure 18. Parallel-coordinate distributions of the Pareto front at different generations.

4.4.3. Statistical Significance Verification

To evaluate the influence of stochastic evolutionary operations on the improved algorithm, 30 independent optimization runs were conducted using the same simulation environment, model parameters, and iteration limit. For each run, the comprehensive fitness was averaged over the final 10 generations, and the resulting 30 run-level values were used for statistical analysis, as presented in Table 8.

Table 8. Objective-specific and comprehensive fitness statistics for 30 independent runs.

Evaluation Index	Mean	Standard Deviation	95% Confidence Interval (Mean ± Half-Width)
Altitude deviation fitness J_1	179.6511744	3.643614303	179.6512 ± 1.3605
Airspeed tracking fitness J_2	113.5151159	0.192502269	113.5151 ± 0.0719
Roll-angle tracking fitness J_3	127.5018972	3.160556157	127.5019 ± 1.1802
Roll oscillation fitness J_4	109.9166751	2.043036515	109.9167 ± 0.7629
Comprehensive fitness	15,3096.09	2816.202201	153,096.09 ± 1051.59

As shown in Table 8, the improved algorithm yielded a mean comprehensive fitness of 153,096.09, with a standard deviation of 2816.20 and a 95% confidence interval of [152,044.50, 154,147.68], showing limited dispersion across the 30 independent runs.

As the comparison baseline, the standard NSGA-II was also evaluated through multiple independent optimization runs under the same settings. It yielded a mean comprehensive fitness of 160,300.37 and a standard deviation of 6952.71. Based on the mean comprehensive fitness values obtained from the repeated runs of the two algorithms, the improved algorithm achieved a relative reduction in mean comprehensive fitness of 4.49%.

The dispersion of the objective-specific fitness values and the performance comparison between the two algorithms are shown in Figure 19. The left panel presents the means and variability of the four objective-specific fitness values using error bars, whereas the right panel compares the mean comprehensive fitness values of standard NSGA-II and the improved algorithm and reports the 4.49% relative reduction.

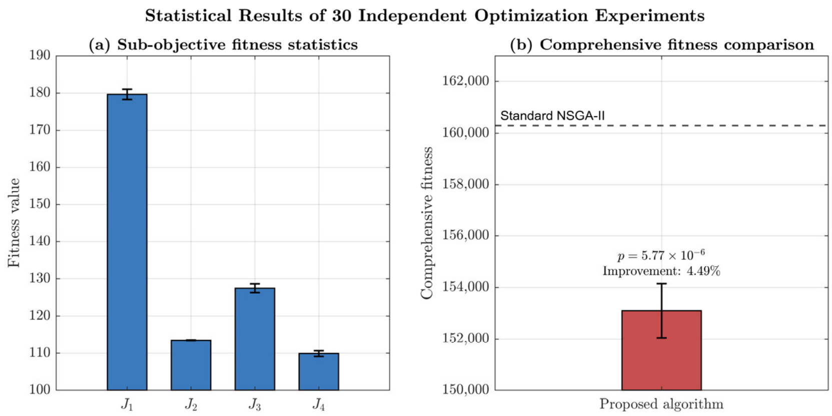

Figure 19. Performance statistics from 30 optimization runs compared with standard NSGA-II.

The mean comprehensive fitness of standard NSGA-II was 160,300.37. According to the unified definition of the relative improvement rate, the improved algorithm achieved a relative reduction of

$$\eta = (J_{base,final} - J_{alg,final}) / J_{base,final} \times 100\% = (160,300.37 - 153,096.09) / 160,300.37 \approx 4.49\% .$$

A two-sided Welch's independent-samples t-test was further conducted to compare the mean comprehensive fitness values of the two algorithms. The test yielded $t = -5.26,\ p = 5.77 \times 10^{-6}$. Since $p < 0.001$, the result supports a lower mean comprehensive fitness for the improved algorithm under the present experimental conditions, consistent with the 4.49% relative reduction.

4.4.4. Computational Cost and Engineering Feasibility Analysis

To quantify the computational cost of offline parameter tuning, the experiments were performed on an AMD Ryzen 7 4800H processor using MATLAB/Simulink R2022b. The total number of simulation calls, simulation step size, and flight-dynamics model were kept identical across all experimental groups for a consistent comparison. The measured average computation time per optimization run was approximately 1.3 h for the standard NSGA-II and 1.4 h for the proposed algorithm, corresponding to a 7.7% increase.

Hierarchical pre-optimization involves numerical operations such as population screening and elite-individual merging and does not add flight-dynamics simulation calls. The higher-quality initial population reduces ineffective evaluations during multi-objective optimization, while the total number of simulation calls remains fixed. The measured 7.7% increase therefore mainly reflects the additional adaptive calculations. Because the hierarchical framework and threefold adaptive mechanism are coupled during iteration, separate module-level timing would not represent the complete procedure.

From an engineering-implementation perspective, the proposed algorithm is used for offline controller parameter tuning on the ground, and the resulting gain-scheduling tables are stored in the flight-control computer. A computation time of approximately 1.4 h per optimization run is compatible with conventional offline parameter development. The computational cost may increase with the dimensionality of the controller parameters. For extensions to full-channel or wider-envelope gain-scheduling tasks, a parallel simulation architecture may be considered to meet the increased computational demand.

4.5. Flight-Test Validation

To evaluate environmental adaptability and engineering feasibility, field flight tests were conducted using a fixed-wing UAV whose main parameters are listed in Table 1. The reference flight altitude was 5500 m. The mean near-ground wind speed was 6–8 m/s with moderate atmospheric turbulence, providing a field disturbance environment broadly comparable to the simulation setting. The onboard attitude sensors operated at 200 Hz, and the flight-control cycle was 0.005 s, consistent with the simulations. Each test item was repeated at least three times to assess repeatability.

For the near-envelope conditions, the roll channel is used as an example to present the optimization results. The six gain-scheduling parameters obtained using the proposed algorithm, namely, k_{pk}, $k_{p\beta 1}$, $k_{p\beta 2}$, b_{pk}, $b_{p\beta 1}$, and $b_{p\beta 2}$, were 0.00098, 0.00095, 0.00063, 3.69, 1.32, and −2.29, respectively. The pitch and yaw channels employed the same dynamic-pressure-based gain-scheduling framework and optimization procedure and exhibited similar convergence characteristics. The procedure was subsequently applied over the tested airspeed range of 60–150 m/s. The resulting scheduling table was loaded into the flight-control computer, followed by level-flight acceleration and continuous-roll tests.

4.5.1. Level-Flight Acceleration and Disturbance-Rejection Test

This test was conducted to evaluate channel decoupling and adaptation to dynamic-pressure variations during level-flight acceleration. At 1260 s, the UAV transitioned from a turn to level flight and accelerated from 70 m/s to 150 m/s while recovering from a -30° left-bank attitude to level flight. The flight-control system selected the optimized parameters from the scheduling table according to the real-time airspeed and applied the corresponding compensation. The results are shown in Figure 20.

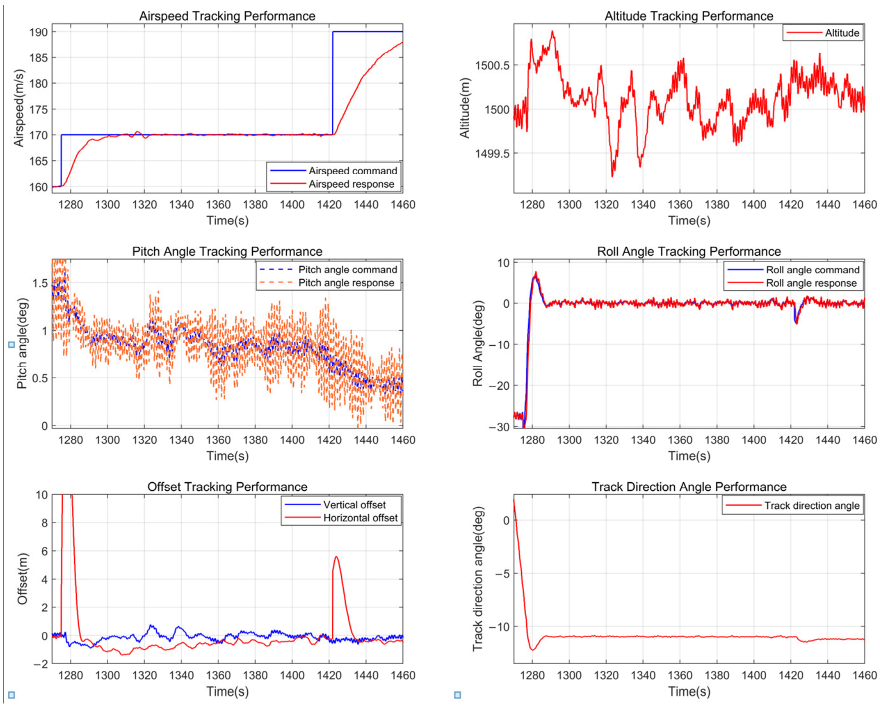

(**a**)

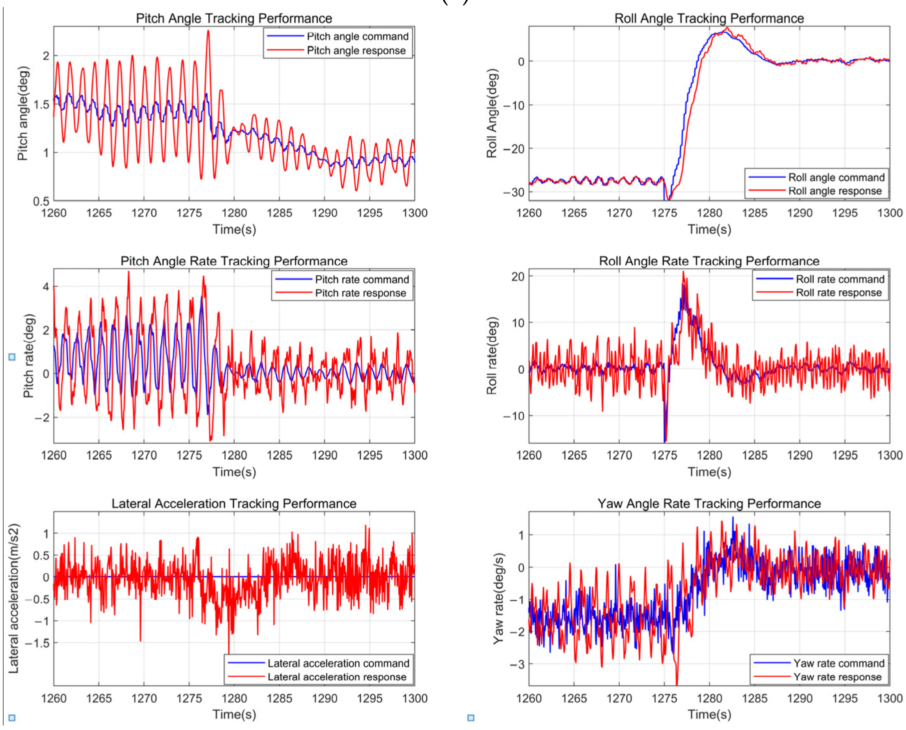

(**b**)

Figure 20. Position and attitude tracking during level-flight acceleration: (**a**) position; (**b**) attitude.

As shown in Figure 20a, during the steady-state level-flight segment, the airspeed error remained within ±0.5 m/s, the altitude variation remained within ±2 m, and the horizontal-track deviation did not exceed ±1 m. After acceleration began, the increase in thrust caused a brief trajectory deviation, after which the UAV converged to the commanded trajectory. No evident delay was observed in the airspeed response to the acceleration command. Altitude and track accuracy remained stable as the aerodynamic parameters varied with airspeed, indicating disturbance-rejection capability in the longitudinal channel.

As shown in Figure 20b, during the steady-state interval from 1260 to 1300 s, the pitch-angle fluctuation remained within ±0.5°, and the steady-state roll-angle error remained within ±1°. The three-axis angular-rate errors remained within ±5°/s, while the pitch- and yaw-rate errors did not exceed ±2°/s. After measurement spikes were removed, the magnitude of the lateral acceleration did not exceed 1 m/s^2. No pronounced attitude transients were observed during acceleration, suggesting reduced aerodynamic coupling between the lateral–directional and longitudinal channels while stable responses were maintained under parameter variations and disturbances.

4.5.2. Continuous High-Bank Roll Maneuvers and Attitude Tracking

This test was conducted to evaluate attitude-tracking and channel-decoupling performance during route transitions and evasive maneuvers. Continuous roll maneuvers with a moderate bank angle of 40° and a high bank angle of 80° were performed. The results are shown in Figure 21.

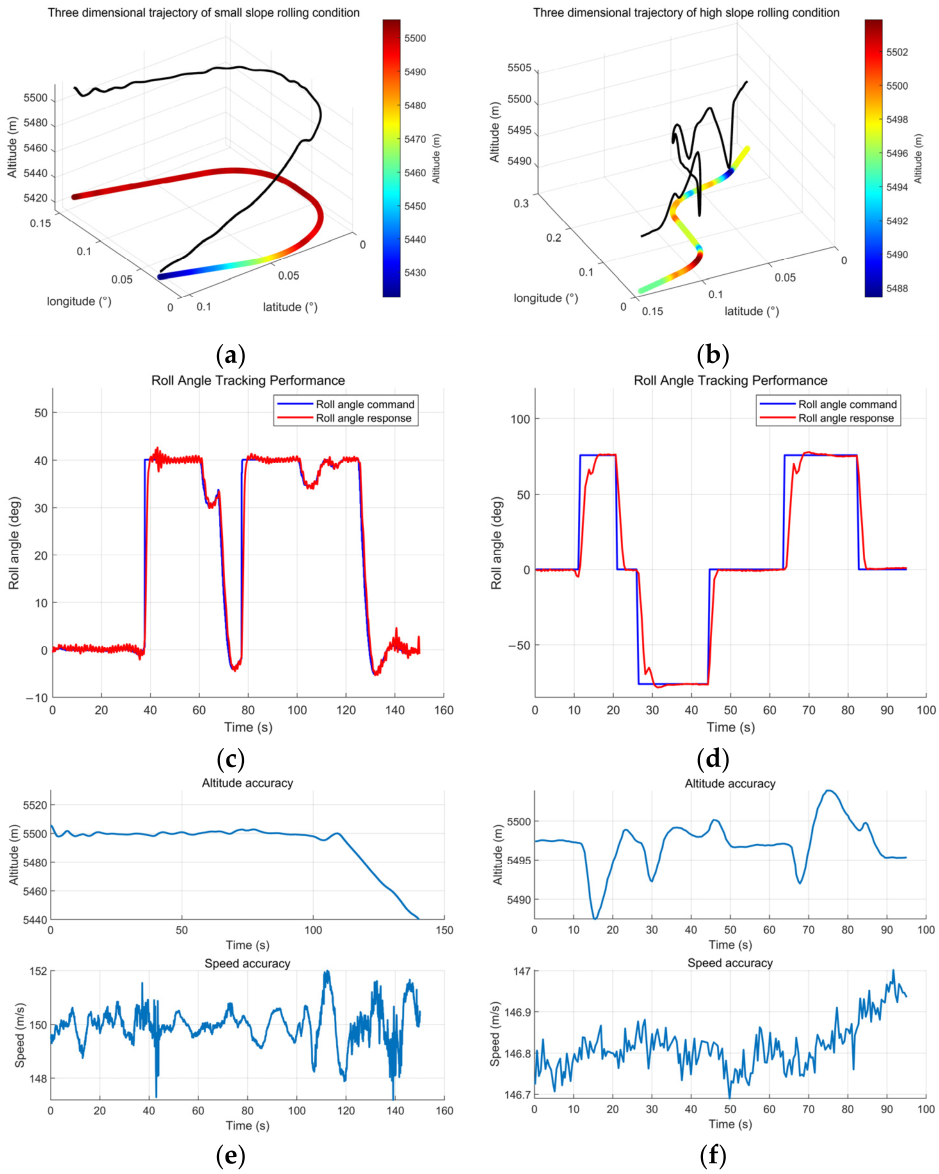

Figure 21. Roll tracking: (**a**) 40° circling trajectory; (**b**) 80° circling trajectory; (**c**) 40° roll response; (**d**) 80° roll response; (**e**) altitude and airspeed variations (40°); (**f**) altitude and airspeed variations (80°).

As shown in Figure 21a,b, the flight trajectories transitioned smoothly during both bank-angle maneuvers, and the turn radii remained stable. No trajectory divergence or high-frequency spatial oscillation was observed, indicating stable roll-channel control.

As shown in Figure 21c,d, the flight-test tracking errors were higher than those in the simulations because of unmodeled aeroelastic effects, servo dead zones, and atmospheric turbulence. At a bank angle of 40°, the roll attitude followed the command with limited overshoot, and only low-amplitude high-frequency fluctuations were observed during the steady-state stage. At a bank angle of 80°, roll-attitude buildup and recovery required approximately 4 s, which was close to the simulation result. No sustained limit-cycle oscillation was observed, which is consistent with the disturbance-compensation role of the linear extended state observer for internal nonlinear disturbances and external wind disturbances.

As shown in Figure 21e,f, after excluding the altitude adjustments caused by manual transitions between test items, the airspeed remained relatively stable and the altitude variation remained within a controllable range during the 40° bank maneuver. During the 80° bank maneuver, the altitude variation increased because of aerodynamic coupling associated with the high-bank turn but remained within the 20 m error band. No sustained altitude loss or divergent trend was observed, indicating that the longitudinal channel attenuated the coupling effects induced by the high-bank maneuver and maintained closed-loop altitude stability.

Overall, the optimized controller maintained attitude-tracking accuracy and longitudinal-state stability during the tested high-bank maneuvers. These flight tests support implementation under the tested conditions; the quantitative improvement relative to experience-based tuning is established by Table 3 and Figures 7–9.

5. Conclusions and Future Work

Overall, the results clarify the distinct contributions of population initialization and adaptive search to near-envelope controller tuning. The main conclusions are as follows.

(1) Multi-objective coordinated optimization performance is improved, but the two algorithmic levels play different roles. Hierarchical pre-optimization alone reduces the mean comprehensive fitness by approximately 4.41% relative to standard NSGA-II. The complete configuration achieves a 4.49% reduction; the three adaptive components provide a further 0.083% reduction relative to hierarchical pre-optimization alone but lower the post-convergence coefficient of variation from 0.0020 to 0.0006, indicating improved convergence stability and consistency.
(2) Disturbance rejection and attitude decoupling under complex operating conditions are verified within the tested ranges. Multi-source perturbation simulations show that the optimized controller maintains stable closed-loop performance under combined aerodynamic, inertial, and actuator perturbations. Near-envelope flight tests further show smooth attitude tracking and bounded altitude and airspeed variations across the tested airspeeds and large-bank roll maneuvers.
(3) The proposed method has engineering implementation potential. The integrated control and optimization framework does not require redesign of the existing flight-control hardware or control-law architecture. Offline coordinated parameter optimization supports controller tuning for the tested fixed-wing UAV under the investigated operating conditions.

Future research will proceed in three directions. First, the pre-optimization procedure and adaptive mechanisms will be simplified to reduce computational cost, and online parameter tuning under limited onboard computing resources will be investigated. Second, a distributed/federated extension will be investigated for multi-UAV systems, in which globally aggregated parameter information provides a common initialization while each UAV retains local adaptation to regional aerodynamic and disturbance conditions [31]. Communication cost, heterogeneous local operating data, and closed-loop safety constraints will also be considered. Third, flight-control-oriented multi-objective optimization mechanisms and evaluation standards will be further investigated for broader platform and operating-condition studies.

Author Contributions: Conceptualization, W.C. and S.G.; methodology, W.C., S.G., X.L., S.W. and Z.W.; validation, formal analysis and investigation, W.C., S.G., X.L., S.W., Z.W., X.J. and Z.Y.; writing—original draft preparation, W.C.; writing—review and editing, W.C. and S.G.; supervision, X.L., S.W., Z.W., X.J. and Z.Y.; project administration, S.W., Z.W., X.J. and Z.Y. All authors have read and agreed to the published version of the manuscript.

Funding: This research received no external funding.

Data Availability Statement: The data presented in this study are available on request from the corresponding author.

Conflicts of Interest: The authors declare no conflicts of interest.

References

1. Zhang, X.; Xue, W.; Liu, Z.; Zhang, R.; Li, H. Compensated Acceleration Feedback Based Active Disturbance Rejection Control for Launch Vehicles. *Chin. J. Aeronaut.* **2024**, *37*, 464–478. https://doi.org/10.1016/j.cja.2023.12.026.
2. Khadraoui, S.; Fareh, R.; Baziyad, M.; Elbeltagy, M.B.; Bettayeb, M. A Comprehensive Review and Applications of Active Disturbance Rejection Control for Unmanned Aerial Vehicles. *IEEE Access* **2024**, *12*, 185851–185868. https://doi.org/10.1109/ACCESS.2024.3510557.
3. Liu, C.; Chen, W.-H. Disturbance Rejection Flight Control for Small Fixed-Wing Unmanned Aerial Vehicles. *J. Guid. Control Dyn.* **2016**, *39*, 2810–2819. https://doi.org/10.2514/1.G001958.
4. Gong, J.; Fan, Y. Active Disturbance Rejection Control Method for UAV Autonomous Aerial Refueling Based on Reflected Pigeon-Inspired Optimization. *Sci. Sin. Technol.* **2025**, *55*, 893–905. https://doi.org/10.1360/SST-2024-0228.
5. Wang, B.; Yan, Y.; Xiong, X.; Han, Q.; Li, Z. Attitude Control of Small Fixed-Wing UAV Based on Sliding Mode and Linear Active Disturbance Rejection Control. *Drones* **2024**, *8*, 318. https://doi.org/10.3390/drones8070318.
6. Wang, Z.; Zhao, H.; Duan, D.; Jiao, Y.; Li, J. Application of Improved Active Disturbance Rejection Control Algorithm in Tilt Quad Rotor. *Chin. J. Aeronaut.* **2020**, *33*, 1625–1641. https://doi.org/10.1016/j.cja.2020.01.002.
7. Yin, Z.; Du, C.; Liu, J.; Sun, X.; Zhong, Y. Research on Autodisturbance-Rejection Control of Induction Motors Based on an Ant Colony Optimization Algorithm. *IEEE Trans. Ind. Electron.* **2018**, *65*, 3077–3094. https://doi.org/10.1109/TIE.2017.2751008.
8. Messac, A. Physical Programming: Effective Optimization for Computational Design. *AIAA J.* **1996**, *34*, 149–158. https://doi.org/10.2514/3.13035.
9. Deb, K.; Pratap, A.; Agarwal, S.; Meyarivan, T. A Fast and Elitist Multiobjective Genetic Algorithm: NSGA-II. *IEEE Trans. Evol. Comput.* **2002**, *6*, 182–197. https://doi.org/10.1109/4235.996017.
10. Zhao, Z.; Liu, B.; Zhang, C.; Liu, H. An Improved Adaptive NSGA-II with Multi-Population Algorithm. *Appl. Intell.* **2019**, *49*, 569–580. https://doi.org/10.1007/s10489-018-1263-6.
11. Chi, P.; Liu, C.; Zhao, J.; Wu, K.; Wang, Y. Dynamic Effect Web Generation for Heterogeneous UAV Cluster Using DQN-Based NSGA-II: Methods and Applications. *Chin. J. Aeronaut.* **2025**, *38*, 103351. https://doi.org/10.1016/j.cja.2024.103351.
12. Zhao, Y.; Lu, J.; Yan, Q.; Lai, L.; Xu, L. Research on Cell Manufacturing Facility Layout Problem Based on Improved NSGA-II. *Comput. Mater. Contin.* **2020**, *62*, 355–364. https://doi.org/10.32604/cmc.2020.06396.
13. Ghambari, S.; Golabi, M.; Lepagnot, J.; Brevilliers, M.; Jourdan, L.; Idoumghar, L. An Enhanced NSGA-II for Multiobjective UAV Path Planning in Urban Environments. In Proceedings of the 32nd IEEE International Conference on Tools with Artificial Intelligence (ICTAI), Baltimore, MD, USA, 9–11 November 2020; pp. 106–111. https://doi.org/10.1109/ICTAI50040.2020.00028.
14. Zhu, C.; Zhang, Y.; Chen, R.; Xu, X.; Chen, H.; Ma, X. Potential Energy Recovery Control Strategy of Scissors Aerial Work Platform Using Improved NSGA-II. In *Developments and Applications in SmartRail, Traffic, and Transportation Engineering*; Jia, L., Easa, S., Qin, Y., Eds.; Lecture Notes in Electrical Engineering; Springer: Singapore, 2024; Volume 1209, pp. 710–719. https://doi.org/10.1007/978-981-97-3682-9_65.
15. Chai, R.; Savvaris, A.; Tsourdos, A.; Chai, S. Solving Multi-Objective Aeroassisted Spacecraft Trajectory Optimization Problems Using Extended NSGA-II. In Proceedings of the AIAA SPACE and Astronautics Forum and Exposition, Orlando, FL, USA, 12–14 September 2017; AIAA Paper 2017-5193. https://doi.org/10.2514/6.2017-5193.
16. Meng, S.; Zhao, G.; Che, C. Optimization of an Anti-Recoil Control Scheme Based on Improved NSGA-II for a Deep-Water Drilling Riser after Emergency Disconnection. *Ocean Eng.* **2025**, *316*, 119823. https://doi.org/10.1016/j.oceaneng.2024.119823.
17. Deb, K.; Jain, H. An Evolutionary Many-Objective Optimization Algorithm Using Reference-Point-Based Nondominated Sorting Approach, Part I: Solving Problems With Box Constraints. *IEEE Trans. Evol. Comput.* **2014**, *18*, 577–601. https://doi.org/10.1109/TEVC.2013.2281535.
18. Saborido, R.; Ruiz, A.B.; Luque, M. Global WASF-GA: An Evolutionary Algorithm in Multiobjective Optimization to Approximate the Whole Pareto Optimal Front. *Evol. Comput.* **2017**, *25*, 309–349. https://doi.org/10.1162/EVCO_a_00175.
19. Zhang, L.; Ge, H.; Ma, Y.; Xue, J.; Li, H.; Pecht, M. Multi-Objective Optimization Design of a Notch Filter Based on Improved NSGA-II for Conducted Emissions. *IEEE Access* **2020**, *8*, 83213–83223. https://doi.org/10.1109/ACCESS.2020.2991576.
20. Gomez, N.; Gomez, V.; Paiva, E.; Rodas, J.; Gregor, R. Flight Controller Optimization of Unmanned Aerial Vehicles Using a Particle Swarm Algorithm. In Proceedings of the 2020 International Conference on Unmanned Aircraft Systems (ICUAS), Athens, Greece, 1–4 September 2020; pp. 588–593. https://doi.org/10.1109/ICUAS48674.2020.9213876.

21. He, H.; Duan, H. A Multi-Strategy Pigeon-Inspired Optimization Approach to Active Disturbance Rejection Control Parameters Tuning for Vertical Take-off and Landing Fixed-Wing UAV. *Chin. J. Aeronaut.* **2022**, *35*, 19–30. https://doi.org/10.1016/j.cja.2021.05.010.
22. D'Antuono, V.; De Matteis, G.; Trotta, D.; Zavoli, A. Optimization of UAV Robust Control Using Genetic Algorithm. *IEEE Access* **2023**, *11*, 122252–122272. https://doi.org/10.1109/ACCESS.2023.3325845.
23. Comer, A.M.; Chakraborty, I. Full Envelope Flight Control System Design and Optimization for a Tilt-Wing Aircraft. *J. Am. Helicopter Soc.* **2024**, *69*, 032003. https://doi.org/10.4050/JAHS.69.032003.
24. Ghiglino, P.; Forshaw, J.L.; Lappas, V.J. Online Evolutionary Swarm Algorithm for Self-Tuning Unmanned Flight Control Laws. *J. Guid. Control Dyn.* **2015**, *38*, 772–782. https://doi.org/10.2514/1.G000376.
25. Xu, D.; Deng, Y.; Duan, H. Parameter Tuning for Active Disturbance Rejection Control of Fixed-Wing UAV Based on Improved Bald Eagle Search Algorithm. *Aircr. Eng. Aerosp. Technol.* **2024**, *96*, 1152–1164. https://doi.org/10.1108/AEAT-12-2023-0342.
26. Shams Taleghani, A.; Ghajar, A.; Masdari, M. Experimental Study of Ground Effect on Horizontal Tail Effectiveness of a Conceptual Advanced Jet Trainer. *J. Aerosp. Eng.* **2020**, *33*, 05020001. https://doi.org/10.1061/(ASCE)AS.1943-5525.0001140.
27. Shams Taleghani, A.; Yektaei, S.; Esfahanian, V.; Abdolahipour, S. Experimental Study on the Effects of Sideslip and Rudder Deflection Angles on the Aerodynamics of an Aircraft Vertical Tail at Low Speeds. *Fluids* **2025**, *10*, 277. https://doi.org/10.3390/fluids10110277.
28. Liu, M.; Wu, Y.; Wang, W. Large-Slenderness-Ratio Supersonic Aircraft Lateral–Directional Coupling Dynamics Analysis and Control. *Int. J. Aerosp. Eng.* **2022**, *2022*, 2490675. https://doi.org/10.1155/2022/2490675.
29. Wang, Z.; Hu, L.; Fei, W.; Zhou, D.; Yang, D.; Ma, C.; Gong, Z.; Wu, J.; Zhang, C.; Yang, Y. High-Performance Attitude Control Design of Supersonic Tailless Aircraft: A Cascaded Disturbance Rejection Approach. *Aerospace* **2023**, *10*, 198. https://doi.org/10.3390/aerospace10020198.
30. Yoo, D.; Yau, S.S.-T.; Gao, Z. Optimal Fast Tracking Observer Bandwidth of the Linear Extended State Observer. *Int. J. Control* **2007**, *80*, 102–111. https://doi.org/10.1080/00207170600936555.
31. Yang, M.-S.; Sinaga, K.P. Federated Multi-View K-Means Clustering. *IEEE Trans. Pattern Anal. Mach. Intell*. **2025**, *47*, 2446–2459. https://doi.org/10.1109/TPAMI.2024.3520708.